Phosphenes in space: a study on the interaction between carbon ions and rod photoreceptor

Ph.D. Thesis

Adele Rinaldi

Supervisor: Prof. Livio Narici

Coordinator: Prof. Piergiorgio Picozza

Doctoral thesis submitted to
Physics Department
Faculty of Mathematics, Physics and Natural Science
University of Tor Vergata
Rome, Italy

June 2009

to my children Tommaso and Maura

Phosphenes in space: a study on the interaction between carbon ions and rod photoreceptor

Adele Rinaldi

Abstract

Phosphenes, or light flashes, have been reported by astronauts since the first Apollo flights to the Moon. They are usually described as occurring in the dark and typically before falling asleep. The light flashes are thought to originate as an effect of high-energy particles interacting with the visual system. The study presented in this thesis investigates the hypothesis of a direct excitation of the rod photoreceptors inside the retina and in particular the interaction between carbon ions and rods. Also the retinal and cortical electrophysiological response of mice submitted to carbon ions irradiation have been studied.

This thesis has been developed as a section of the 'Anomalous Long Term Effects on Astronauts' (ALTEA) program, and all the experiments concerning this thesis took place on ground. The objective of the ALTEA project is more general, and is aimed to assess the functional risks on the central nervous system due to particle flux in microgravity conditions during long term space mission. ALTEA includes a series of experiments both in orbit and on ground. The experiments on board International Space Station will contribute to define the causes of the anomalous phosphene perception of the astronauts by detecting the incident particles through the head of the astronauts and concurrently monitoring the central nervous system functionality. The experiments on ground include the direct irradiation with carbon ions of the outer segments of the rods, and an animal model to investigate the retina/cortex responses of mice irradiated in controlled laboratory experiments. In these experiments on ground I directly contributed in the preparation, the test and the optimization of the experiments and in the following analysis of the data. The whole project has been supported by the Italian Space Agency.

The outline of this thesis includes an introduction to the interdisciplinary ALTEA

program in the first chapter.

In the second chapter ALTEA-MICE (Mice intermittent Irradiation with Concurrent Electrophysiological monitoring) study is described: the experimental sessions as well as the evidences in the electrophysiological responses of the mouse retina have been described in detail. My role has been chiefly the experimental set up, and I also collaborated on the data analysis. The main results of this investigations have been published [1], [2].

In the third chapter the system of the rod outer segments in suspension and the mechanism of the activation of the photoreceptors are described.

The fourth chapter deals with the radiation effects in the biological tissue, and in the fifth chapter there is particular regard to the effects of radiation on samples containing a suspension of rods extracted from bovine retinae.

The effects on the rod photoreceptor rhodopsin has been studied: measurements have been performed irradiating with ^{12}C ions the outer segments of the rods in suspension. The amount of the isomeric transformations (*bleaching*) of the molecules of chromophore into the photoreceptor gives the extent of the effects of radiation. I collaborated to the experiment and carried out the following data analysis.

Finally, in the sixth chapter the process of the photo-isomerization of rhodopsin is explained by a model: the process starts with the water radiolysis and the formation of hydroxyl radicals OH in order to achieve the lipid peroxidation, then there is the subsequent emission of visible photons which are responsible for the photoreceptor bleaching. Since rhodopsin is surrounded by phospholipids, present in high concentration in the disc membranes, the effect of chemiluminescence is proposed to be the cause of the photo-transduction cascade and the light flash perception as a consequence. In order to test this hypothesis, a series of experiments was aimed at studying the effects of the hydroxyl radicals produced in an enzymatic way. The main results of this work are illustrated in chapter six, and have been published in [3].

Acknowledgements

I kindly thank ALTEA (*dream*) team, my real second family:

Veronica and Luca, for their open-mindedness, and for the years spent together, day by day, in mutual trust and support; my colleagues Marianna, Chiara, Alessia, Cristian and Monia.

I sincerely thank Livio Narici, my supervisor, for giving to me the opportunity of working in the ALTEA program. He led me to new branches and topics of physics, with his strength and vitality; he has been always present to solve our problems and questions.

I thank Valentina and Angelo, Simone, prof. W. G. Sannita, Prof. M. Paci and Vittorio Bidoli.

Contents

Chapter 1

ALTEA: an investigation on heavy ion effects on nervous system

1.1 Visual phosphenes in space

On the historic July 1969 Apollo 11 mission, astronauts in lunar orbit reported an incidental finding of various starlike flashes, streaks and clouds in their visual field. Actually, astronaut Edwin Aldrin was the first to report phosphenes, or light flashes (LF), in eyes during the space flight [4]. Subsequently, more detailed observation were made on Apollo mission 12-17 and on Skylab 4 flights; during the Apollo-Soyuz test project (ASTP) and on board Mir. Presently, on board International Space Station (ISS) orbiting in the Low Earth Orbit (LEO), crew members perceive LF. Although it is clear that the phosphenes are related to high-energy particles in the space radiation environment, many details about LF origins are still unknown.

The flashes get perceivable usually under dark adaptation conditions. The flashes are usually colorless; only in few cases they are colored. Because of these features, the flashes are commonly accepted to be due mostly to scotopic vision. The different shapes, as reported in some graphic descriptions in [5], are commonly illustrated as stars, double stars, 'supernovas', streaks, 'sky of stars', clouds, bright flashes with halo, and so on, observed, on Apollo, Skylab, and on Mir Station. Apparently they differ from the diffuse glow from X-ray exposure or induced from neutron generators [6]. Early human studies in accelerators [7] also suggest a correlation with

increased particle flux in the eye. On Skylab 4 two dedicated light flash observing sessions were conducted by one of the crewmen during the mission (on January and on February 1974) [8], [9]. The phosphenes were seen only during crew sleep periods at times when the crewmen were awake in their darkened sleep compartments.

On Mir [12], it is much lower (Sileye-1, $0.18 \pm 0.02\, LF/min$; Sileye-2, $0.13 \pm 0.01\, LF/min$) than on Apollo [13] ($0.23 \pm 0.01\, LF/min$), Skylab [14] ($1.3 \pm 0.1\, LF/min$) and ASTP [15] ($0.46 \pm 0.05\, LF/min$). Frequency occurrence of LF is up to 25 times higher near the magnetic poles than in equatorial latitudes. In general, the suggested explanation for LF was in terms of interaction between cosmic ray particles and the eye.

Reference [16] is a study initiated to collect information from people who have recently flown in space. It is a survey conducted by anonymous questionnaire and was performed among astronauts regarding their experience of sudden LF in space. In all, 98 surveys were distributed to current NASA and ESA astronauts. Among the 59 respondents, 47 noticed them sometime during space flight. Most often they were noted before sleep, and several people even thought the LF disturbed their sleep. There is an increase of occurrence with orbital altitude and inclination, as one would expect from the increased particle fluxes there. The LF predominantly appear white, but other colors are mentioned, pale green, blue and in particular yellow (10%); they have elongated shapes, and most interestingly, often come with a sense of motion. The motion is described as sideways or in-out, but never in the vertical direction.

Interest in the flashes has arisen from the practical and fundamental significance of the phenomenon. The practical aspect embraces the radiation safety, in-flight rest, and capacity for work of astronauts in long-term and distant space flights. Long travels outside the shielding magnetosphere are also being considered, with the Moon and Mars as next plausible targets. Health risks due to microgravity and cosmic radiation should nevertheless be expected to increase.

Almost all manned flights took and take place in LEO, at altitudes varying between 200 and $500\, km$, with the only exception of the Apollo program, which took man on the Moon and outside Earth's geomagnetic shielding. Most LEO

missions (such as Mir, ISS and Shuttle) have a low inclination (51.6° with respect terrestrial axis) to avoid high latitude areas, where the lower geomagnetic cutoff results in a higher cosmic ray flux [17]. Cosmic rays and radiation measurements inside spacecraft have been the subject of intense investigations throughout the course of space exploration. These studies are particularly difficult since they need to take into account the orbit dependence of cosmic ray flux and its propagation inside the varying absorber thicknesses of the spacecraft.

The biophysics of particle action and the visual structures/functions eventually involved in the generation of phosphenes remained undefined. The aims of the SilEye-1, SilEye-2, Alteino experiments were to investigate this phenomenon: they are the precursors of the ALTEA experiments. SilEye-1 and SilEye-2 experiments [18] performed LF observations on board Mir space station in the years 1995-1999; a total of 18 hours of observation in 19 sessions resulted in the observation of 145 LF. SilEye-2 consists of a silicon detector telescope coupled to a 'helmet' with an eye mask, worn by the astronauts to carry out LF observations [10]. ISS data have been taken in 2002 with Alteino device [19] during the Soyuz-34 flight. Alteino was composed of two distinct devices: the cosmic ray advanced silicon telescope and an ElectroEncephaloGrapher (EEG). Alteino project helped set the experimental baseline for the ALTEA experiments, while providing novel information on the radiation environment onboard ISS and on the brain electrophysiology of the astronauts during orbital flights [20] [21].

1.2 The ALTEA program

ALTEA is a multidisciplinary project (including sub-projects such us ALTEA-mice experiments, ALTEA-biophys) carried on with international collaborations. The project has been financed by the Italian Space Agency (ASI) with the collaboration of the National Institute for Nuclear Physics (INFN) and rated 'Highly recommended' by the European Space Agency (ESA).

The ALTEA facility is available to the international scientific community for human electrophysiological experiments, studies on particle flux, and dosimetry in

the ISS; the ALTEA hardware has been operating in the ISS - USLab since August 2006. It improves the particle observation capabilities of its precursors SilEye and Alteino detectors while performing an advanced electrophysiological monitoring of the Central Nervous System (CNS) during long orbital flights.

The ALTEA space particle detector is a natural development of previous SilEye and Alteino detectors, with a much larger solid angle coverage for the particles passing through the head. To obtain objective information about the LF perception we included in the system the possibility of recording electrophysiological signals via a high definition EEG. To monitor the status of the visual system in microgravity a visual stimulator was also added. Correlations between electrophisiological changes and passages of particles through the brain and/or retina in the space-adapted conditions have been studied.

The detector system consists of an helmet shaped mechanical structure holding 6 advanced silicon telescopes to monitor incoming comic rays, an EEG to monitor brain activity and a visual stimulator, to determine the functional status of the visual system and study its dynamics. The silicon particle telescopes will be positioned over the whole cerebral cortex. Each telescope is made of six silicon planes, and each plane contains two contiguous basic sensor; the basic sensor is obtained assembling back to back two chips with ion implanted resistive strips, $8 \times 8\, cm^2$ of sensitive area, $380\, \mu m$ thick, strip pitch of $2.4\, mm$. To allow both x and y coordinate measurement the strips of the two detectors are perpendicular.

The EEG system will measure the concurrent changes in the cortical bioelectrical activity; it is made up of a 32 electrode EEG cap including three floating electrodes for retinogram measurements, and high resolution electronics allow for electrophysiological readings. The visual stimulator, used to deliver standard stimuli, will permit to perform suitable stimulation routines, to determine the status of the visual system. A three-button pushbutton is used to signal the LF perception. At the highest sensitivity, the silicon detector system is able to detect particles from He to relativistic Mo, and protons between 25 and $200\, MeV$ [22]. All information will be stored together via an integrated data handling system that will also allow transmission of the data to ground [23].

The ALTEA program includes ground-based experiments which are a series of experiments based on measurements in particle accelerators. In the following sections 1.5 and 1.4 ALTEA-MICE and ALTEA-biophys are explained in detail.

1.3 The ALTEA facility on board International Space Station

Figure 1.1: 8 March 2007. Astronaut Sunita Williams, Expeditions 14 and 15 Flight Engineer, receives assistance from Astronaut Michael Lopez-Alegria, Expedition 14 Commander, in donning the sensor studded cap as she prepares to calibrate equipment for the Anomalous Long Term Effects in Astronauts' Central Nervous System experiment in the Destiny laboratory module, image NASA ISS014E16195.

ALTEA space is mounted on an express rack in the USLab and can be utilized in two modalities: dosimetry (DOSI) and central nervous system monitoring (CNSM) [9].

In the DOSI unmanned modality, the six detectors on the helmet (silicon detector system, SDS), continuously measure the environmental radiation. Data are

Figure 1.2: 8 March 2007. Astronaut Sunita Williams, Expeditions 14 and 15 Flight Engineer, wears the Anomalous Long Term Effects in Astronauts' Central Nervous System experiment helmet while conducting the experiment in the Destiny laboratory module, image NASA ISS014E16208.

downlinked in real time to the ground, to the User Home Base in the Department of Physics of the University of Rome Tor Vergata. Real time and off line software provides tools to discriminate the kinds of particles, calculate trajectories and energy of the particles, constructing spectra of the measured radiation. ALTEA operated in DOSI mode almost continuously from August 2006 to July 2007.

The manned experimental modality (CNSM) is specifically aimed at the study of the interaction between particle passages and brain electrophysiological dynamics. The detector is extended normal to the rack. The astronaut wears the EEG cap (see figure 1.1), inserts the disposable pregelled electrodes, slides into the SDS helmet and wears the visual stimulator which also permits dark adaptation. In this con-

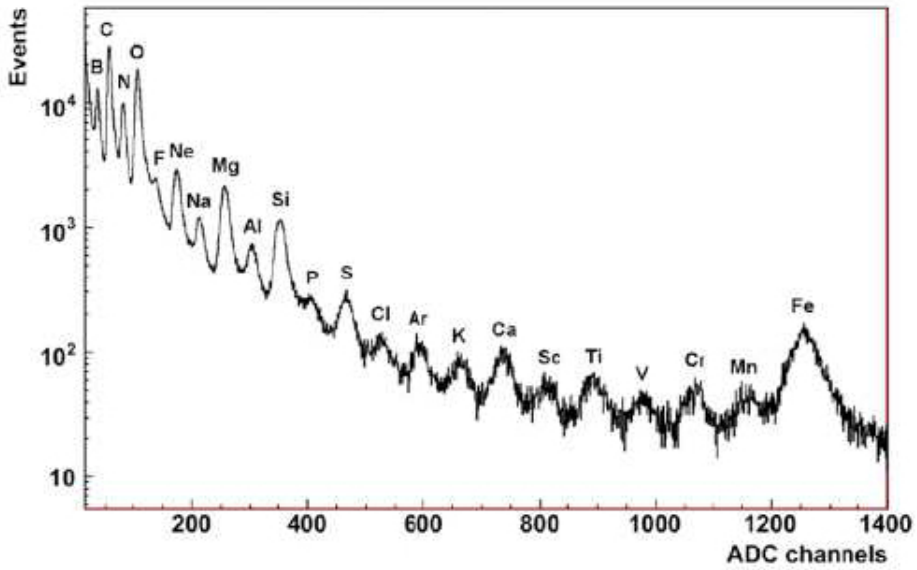

Figure 1.3: A spectrum of the radiation environment into the USLab of the ISS. From [9].

figuration, the SDS measures the particles passing through the astronauts head(see figure 1.2). For about $25\,min$ he/she is presented with a standard set of visual stimuli, then the astronaut relaxes; after about $5 - 10\,min$ of dark adaptation the observing session starts: each perception of a LF is signaled with the pushbutton. The observing session lasts about one hour. Total measurement time is about $1.5\,h$: one orbit. Seven sessions with three astronauts have been performed. The last one was lengthened to allow a measurement with a full passage in the SAA (the other six did not pass over the SAA during the observing time).

In the figure1.3 a measured spectrum of the radiation environment into the US-Lab is shown. The spectum contains only fast particles, which releases an almost constant energy (that is that the difference in released energy between the two outer planes of the silicon telescope is $< 10\%$). The plotted data refer to about six months acquisition with 10 MIP threshold, where MIP means Minimum Ionizing Particle $1\,MIP = 109\,keV/380\mu m$ of silicon.

1.4 ALTEA-biophys rationale and experiments

The ALTEA-biophys section of the ALTEA program is a set of ground-based experiments direct, in particular, to search for answers to the question: what are the specific (or one of the possible) interactions causing the functional effects of the LF?

As explained in section 2.1, rhodopsin is at the start of the phototransduction cascade in the process of vision. It is one of the best molecular transducers for converting a visible photon into an electric signal. It is therefore the first candidate as the target for the radiationvisual system interaction. For this purpose we started *in vitro* investigations of the behavior of rhodopsin when hit by heavy ions. We have been working to study the possibility that rhodopsin can also be activated by irradiation with ^{12}C nuclei. Intact rod outer segments (ROS) containing rhodopsin were isolated from bovine retina. Suspended ROS were irradiated with ^{12}C ($200\,MeV/n$, well below the Cherenkov threshold, see section 3.2) at GSI. Spectrophotometric measurements investigated the activation (bleaching) of the rhodopsin. With these measurements we were able to show that radiation can induce bleaching.

1.5 ALTEA-MICE rationale and experiments

We set up an animal model using mice, irradiated with very short bursts of heavy ions while concurrently acquiring electrophysiological data from the retina and from the cortex. MICE is the acronym for *Mice intermittent Irradiation with Concurrent Electrophysiological monitoring.*

ALTEA-MICE investigates the effects of heavy ions on the visual system of both normal mice and mice with gene defects affecting retinal sensors. The experimental main goal is to develop an animal model to better understand human risk related to particle exposure. The experiments are expected to provide background information that will supplement the ALTEA project on astronauts' safety. ALTEA-MICE also helps identify reliable laboratory conditions comparable in important respects to those of astronauts in space and suitable for further investigations. Experiments have been performed at the Brookhaven National Laboratories (BNL - Upton, NY, USA), with NASA support, and at the Gesellschaft fur Schwerionenforschung mbH

(GSI)/Biophysik (Darmstadt, FRG), with application of standardized methods to identify electrophysiological changes in visual structures in response to pulse radiation [2].

Chapter 2

The rod outer segment and the chromophore of the rhodopsin protein

The evidence of the LF perceptions correlated to heavy ion exposition of the retina does not solve the problem of the biochemical generation of this perception, for this reason a section of the ALTEA program has been devoted to study a selected way of radiation interaction with the visual system. This study originates from the long experiences of SilEye, Alteino, and the collections of the experiments performed in the 70's in space and on ground, all summarized in [9].

ALTEA-biophys investigates the effects of the carbon ion irradiation on the photoreceptors extracted from the bovine retina. The focus point of ALTEA-biophys is the rod photoreceptor (rhodopsin); the retinal, bound to rhodopsin photoreceptor, is at the starting point of the scotopic vision [24], and, following a physiological path, could be the starting point of the LF sensation. In the following this hypothesis will be investigated, the results will show its validity as a possible cause of LF.

The retinal is the light-absorber part of the rhodopsin, that is the chromophore, responsible for the primary absorption, and whose presence is responsible for the light-pink color of the whole molecule. The retinal is a photo-sensitizer because it is at the origin of the reaction generated by light, which does not occur in the absence of the sensitizer. In particular, in this case, as shown in this chapter, the

retinal undergoes photo-isomerization, where starting and end-product differ only in their sterical configuration. On the other hand, when radiation interact with matter and in particular with living tissue, chemical reactions are caused by ionizing radiations, but the absorption is not selectively restricted to certain molecules, like the chromophore, but involves the system as a whole. So, as a starting point, it's not trivial to focalize a specific path for the radiation activation of a visual perception.

2.1 Rods and rhodopsin photoreceptor

The retina [25] is a filmy piece of tissue, barely half a millimeter thick, that lines the inside of the eyeball. It includes both the sensory neurons that respond to light and intricate neural circuits that perform the first stages of image processing; ultimately, an electrical message travels down the optic nerve into the brain for further processing and visual perception, and the retina is therefore considered part of the brain. The sensory cells, the photoreceptors, lie at the very back of the retina; light rays must pass through the entire retina before reaching pigment molecules to excite. This is because the pigment-bearing membranes of the photoreceptors have to be in contact with the eye pigment epithelial layer, which provides a steady stream of the vital molecule, retinal (RET) or vitamin A.

The vertebrate retina contains two different photoreceptor cells: rods and cones. The first are associated with scotopic (nocturnal, achromatic) vision while cones, featuring lower sensitivity to lights, are associated with photopic (diurnal, chromatic) vision. Rodents such as rats and mice, which are nocturnal animals, still have retinas overwhelmingly dominated by rods; their cones are small in size and only make up 3 to 5 percent of their photoreceptors.

The rod cell [27] has a thin shape, approximately $40\,\mu m$ long and $1\,\mu m$ of diameter. It is a neuron whose outer segment is specialized for photoreception. As depicted in figure 2.1 at the base of the rod cell there is a synaptic terminal. Its inner segment contains the cells metabolic machinery. Rhodopsin is synthesized in the inner segment and is transported to the outer segment where it is incorporated into the plasma membrane; it is one of the best molecular transducer system to

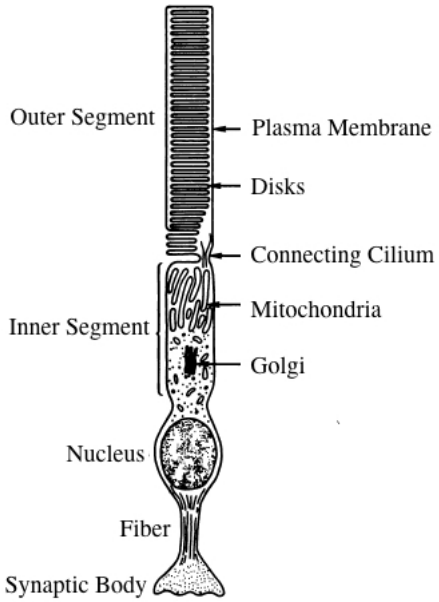

Figure 2.1: Rod cell of the vertebrate retina. From [27].

convert a visible photon into an electric signal. Intracellular disk membranes are formed by evagination and pinching off of the plasma membrane. The outer segment include approximately one thousand disks and each disk is about $16\,nm$ thick. The disk membranes are 50% lipid and 50% protein; 90% of their intrinsic membrane protein is rhodopsin. In the stack of rod outer segment disks enclosed by the plasma membrane, rhodopsin concentration is as high as $3.5\,mM$.

The protein is presented as a bundle of seven helices that traverse the membrane and provide a binding pocket for retinal. In addition to the chromophore, discussed below, rhodopsin is modified by two palmitoyl groups at Cys-322 and Cys-323 in the cytoplasmic region; rhodopsin is also modified by two carbohydrate moieties at Asn-2 and Asn-15 that are oriented toward the extracellular face[1] [28]. Figure 2.2 provides the secondary structure diagram of bovine rhodopsin.

As a visual pigment, rhodopsin displays many specialized features: in particular, visual pigments are made of an opsin [2] and a 11-*cis* retinal chromophore (see figure

[1]For this reason photoreceptor glycoprotein refers to rhodopsin.

[2]Opsins are a group of light-sensitive 35-55 kDa membrane-bound G protein-coupled receptors of the retinylidene protein family found in photoreceptor cells of the retina.

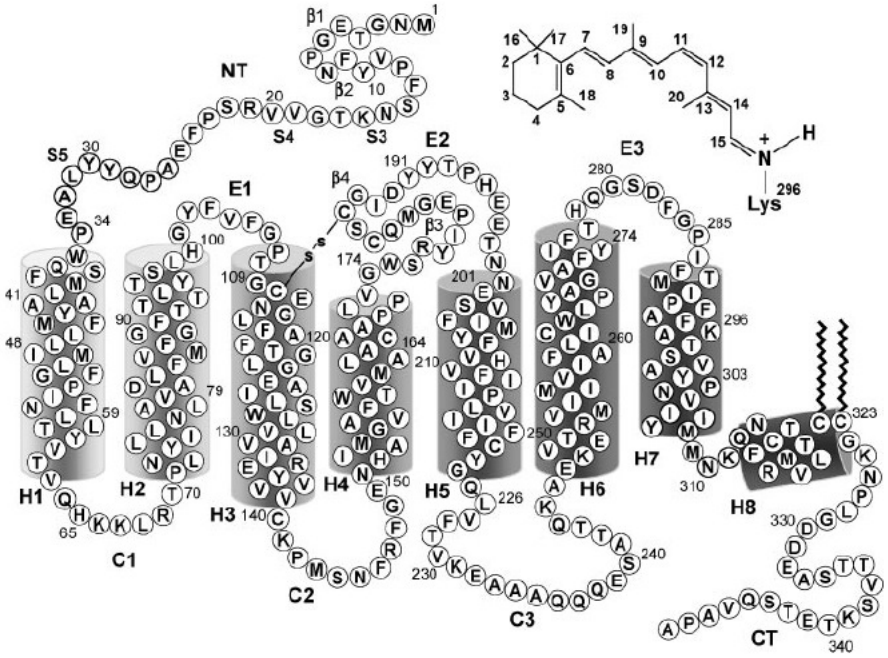

Figure 2.2: A secondary structure diagram of bovine rhodopsin. Amino acid residues are depicted in single-letter code. The amino-terminal tail and extra-cellular domain is toward the top, and the carboxyl-terminal tail and cytoplasmic domain is toward the bottom. Transmembrane α-helical segments (H1 to H7) and the cationic amphipathic helix H8 are shown in cylinders. An essential disulfide bond links Cys-110 and Cys-187. Cys-322 and Cys-323 are palmitoylated. (Inset) The structure of the RET chromophore. Carbon atoms are numbered 1 through 20. From [26].

2.2). The chromophore is not a ligand in the classical sense because it is linked covalently via a protonated Schiff base bond in the membrane-embedded domain of the protein. The Lys residue that acts as the linkage site for the chromophore (Lys-296) is conserved within H7. A carboxylic acid residue that serves as the counterion to the protonated, positively charged retinylidene Schiff base (Glu-113) is conserved within H3. As we have mentioned previously, absorption of light by bound ligand of the rhodopsin, 11-*cis* retinal, causes it to be isomerized to the all-*trans* isomer and is the primary event in visual signal transduction, and it is the only light-dependent step. Isomerization of retinal leads eventually to the thermal decay of

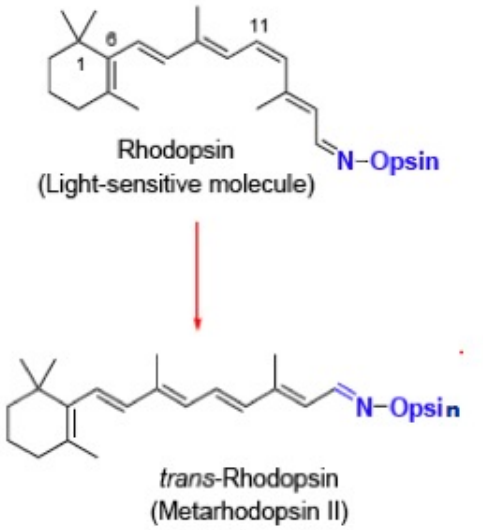

Figure 2.3: Photo-isomerization of the retinal. 11-*cis* retinal, responsible of the light-pink color of the molecule, is isomerized (*bleaching*) to the all-*trans* isomer, which is colorless.

the opsin-retinal complex to yield the protein opsin and free all-trans retinal. The receptor activation process occurs in milliseconds through a series of intermediates distinguished by their spectral characteristics, yielding Metarhodopsin I, which then forms Metarhodopsin II, the retinal conformation is schematically depicted in figure 2.3. Rhodopsin displays a broad visible absorption maximum (λ_{max}) at about $500\,nm$, as shown in figure 2.4. The red circle in the figure indicates the *isosbestic point* which correspond to a wavelength at which the absorption of light by a mixed solution remains constant as the equilibrium between the components in the solution changes.

2.2 ROS preparation from bovine retinae and spectroscopic measurements

Rods have been isolated according to a procedure modified from [29] and [30], using fresh bovine retinae excised from eyes. A single bovine retina may contain as much as $\approx 800\,\mu g$, or $\approx 20\,nmol$, of rhodopsin. We used samples of intact bovine rod

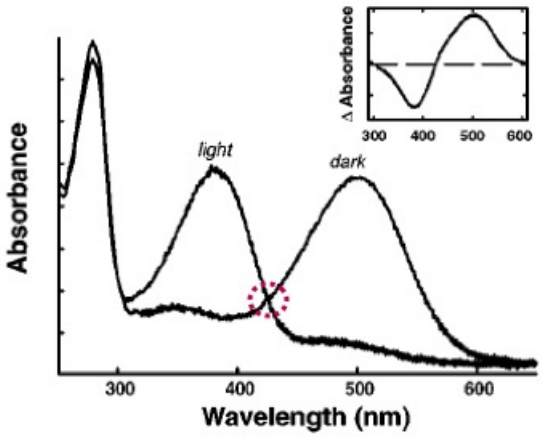

Figure 2.4: A UV-visible absorption spectrum shows a characteristic broad visible absorbance with $\lambda_{max} \simeq 500\,nm$. The $280\,nm$ peak represents the protein component. After exposure to light, the pigment is converted to metarhodopsin II with $\lambda_{max} \simeq 380\,nm$ characteristic of an unprotonated Schiff base imine. The red circle put on view an isosbestic point around $420\,nm$. *Inset*: The photo-bleaching difference spectrum obtained by subtracting the light spectrum from the dark spectrum. From [26]

outer segments [31] in suspension. All sequential steps for ROS preparation were conducted under dim red light conditions at room temperature. Rhodopsin concentration was spectroscopically determined by using a molar extinction coefficient value $\epsilon_{500nm} = 40.600\,M^{-1}cm^{-1}$ [32], and a molecular weight of $40.000\,D$. ROS suspension in Ficoll 5%w/w (Sigma)[3] was stored at $-80°C$ till use [33], [3].

To check the integrity and functionality of rhodopsin, we spectroscopically monitored the absorption of the ROS suspension (wavelength range: $400\,nm \div 650\,nm$), before and after light exposure. The following is a brief explanation of these measurements. In a spectrophotometer, monochromatic light enters a sample at right angles to the plane-surface of the sample. In these conditions, the transmittance and absorbance of a sample depends on the molar concentration c, light path length in centimeters L, and molar absorptivity ϵ for the dissolved substance. Beer's Law

[3]Ficoll is a neutral hydrophilic polysaccharide which dissolves readily in aqueous solutions.

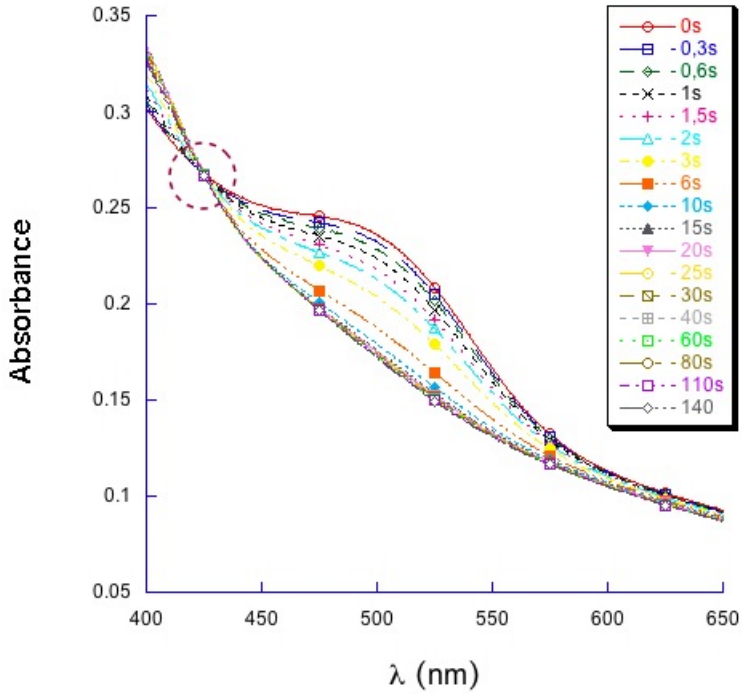

Figure 2.5: Absorption spectrum shows a characteristic peak at $\lambda_{max} \simeq 500\,nm$. During the exposure to light, the pigment isomerizes and the peak comes down. In the circle the isosbestic point at $\approx 425\,nm$.

states that molar absorptivity is constant and the absorbance is proportional to concentration for a given substance dissolved in a given solute and measured at a given wavelength. Standard laboratory spectrophotometers are fitted for use with $1\,cm$ width sample cuvettes; hence, the path length L is generally assumed to be equal to one centimeter. The next equations provide a summary of these simple concept

$$A = Log\,\tfrac{1}{T} = Log\,\tfrac{I_0}{I} \quad \text{where} \begin{cases} A\text{: absorbance} \\ T\text{: transmittance} \\ I_0\text{: intensity of the incident light} \\ I\text{: intensity transmitted through sample} \end{cases} \tag{2.1}$$

$$\epsilon = \frac{A}{c \cdot L} \quad \text{where} \begin{cases} \epsilon\text{: extinction coefficient (or molar absorptivity)} \\ c\text{: concentration } (mol/l) \\ L\text{: path length } (cm) \end{cases} \tag{2.2}$$

In figure 2.5 we show the measured absorption spectrum for one of our prepared sample of ROD in suspension. The sample have been exposed to the light of a white LED[4], inserted in the top of the cuvette holding the suspension. The compound shows the characteristic maximum absorbance at $\lambda_{max} = 500\,nm$ required by the presence of the 11-cis-retinal. During successive exposures to light, the peak comes down until all the retinal is bleached. In the same plot the dotted circle shows the expected isosbestic point at circa $425\,nm$.

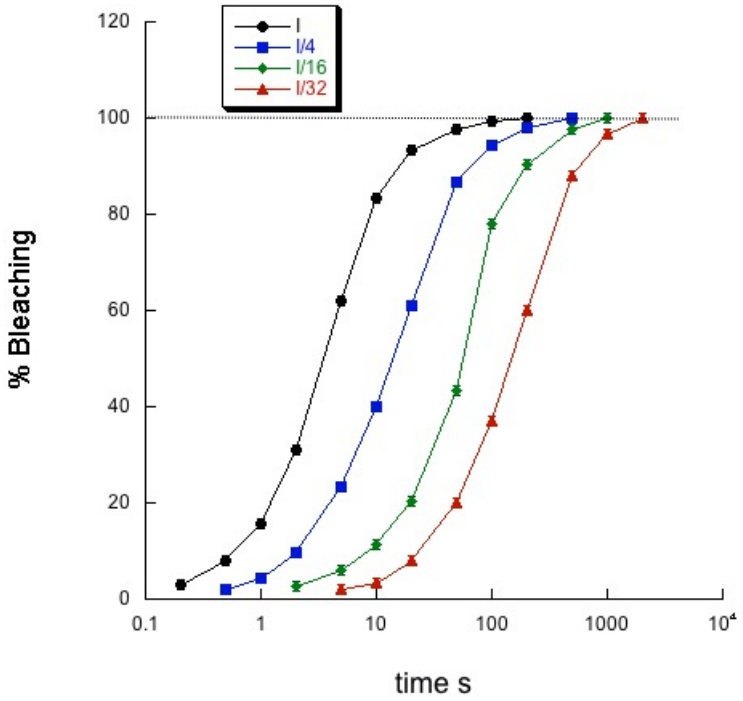

Figure 2.6: Rhodopsin bleaching in percent as a function of the time of exposure to light (in a semi-logarithmic plot). Four samples were exposed to different intensities of light, with respect to a given intensity I, that is I, $I/4$, $I/16$ and $I/32$.

[4]From RS catalogue: $I(i) = 3000\,mcd$; $V = 3.6\,V$; $i = 20\,mA$; $i_{max} = 30\,mA$.

From the spectrum displayed in figure 2.5 is possible the calculation of the amount of the 11-cis- retinal, unbleached rhodopsin, as a results of the relations 2.1 and 2.2. The molar concentration is given by the ratio of the difference in absorbance in the dark (before exposure to light) and the absorbance after a sufficient long exposure (when the retinal is completely bleached), and the extinction coefficient at the same wavelength $\lambda_{max} = 500\,nm$

$$c = \frac{A_{500nm}^{unbleached} - A_{500nm}^{bleached}}{\epsilon_{500nm} \cdot L} = \frac{A_{500nm}^{unbleached} - A_{500nm}^{bleached}}{40600} \tag{2.3}$$

the error propagation gives

$$\Delta c = \frac{\Delta A_{500nm}^{unbleached} + \Delta A_{500nm}^{bleached}}{40600} \tag{2.4}$$

considering the absorbance error $\Delta A = 0.0002$ that is twice the instruments sensitivity. Using these calculations for the sample in figure 2.5, for example, we obtain the concentration of the 11-cis-retinal (active rhodopsine) available before exposure to light $(c = 1.62 \pm 0.01)\,\mu M$.

In figure 2.6 the rhodopsin bleaching in percent is displayed as a function of the time of exposure to different intensities of light. Assuming that the luminous intensity I given by the LED is proportional to the electric current i, we modulated four different light intensities to obtain the values I, $I/4$, $I/16$, $I/32$, corresponding respectively to nearly $3000\,mcd$, $750\,mcd$, $188\,mcd$ and $94\,mcd$.

The same curves displayed in figure 2.7 are re-scaled and plotted in figure 2.7, where the bleaching is in function of the radiant energy, expressed in an arbitrary scale. In this way, taking into account the different light intensities and dividing the exposition times by the correct factor, we obtain the superimposition of the four curves. In the inset of the figure 2.7 the horizontal axis is in linear scale. Thus, we can say that in our experimental conditions the percentage of the bleaching of rhodopsin present in our samples depends on the energy delivered, not depending on the time of exposition and the intensity of light (expressed in cd in our experiments).

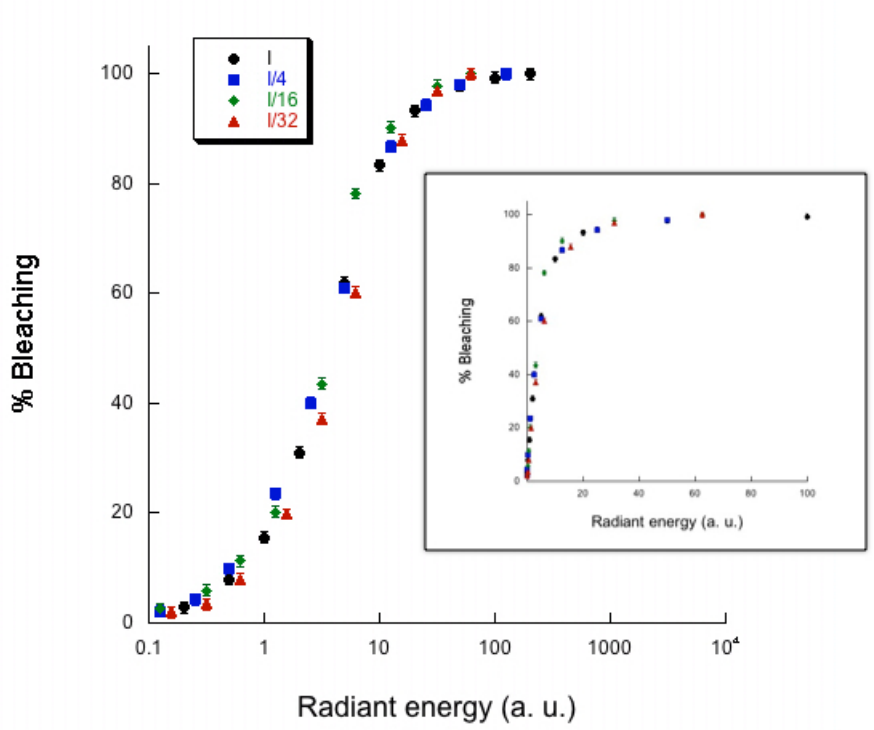

Figure 2.7: Rhodopsin bleaching in percent as a function of the radiant energy in a semi-logarithmic scale, and (*inset*) in linear scale. The radiant energy is in arbitrary units.

2.3 11-*cis*-retinal regeneration

To check the integrity and functionality of rhodopsin, we spectroscopically monitored the absorption of the ROS suspension, before and after light exposure. After the total light bleaching, rhodopsin was regenerated by the addition of 11-*cis* retinal (kindly provided by the National Eye Institute, USA) at the suspension. 11-cis retinal was added 3:1 with respect of rhodopsin concentration and then the reaction was stopped after 15 minutes of incubation by the addition of 10 mM hydroxylamine (Sigma) [33]. After the regeneration, a second light bleaching was performed. The absorbance differences at 500 nm, before and after rhodopsin regeneration, provided us the total regeneration percentage (typically better than 95%). We also checked the thermal stability of ROS suspension both at room temperature and after subsequent freezing and thawing [33].

Figure 2.8 shows the spectra of the unbleached and bleached sample, before and

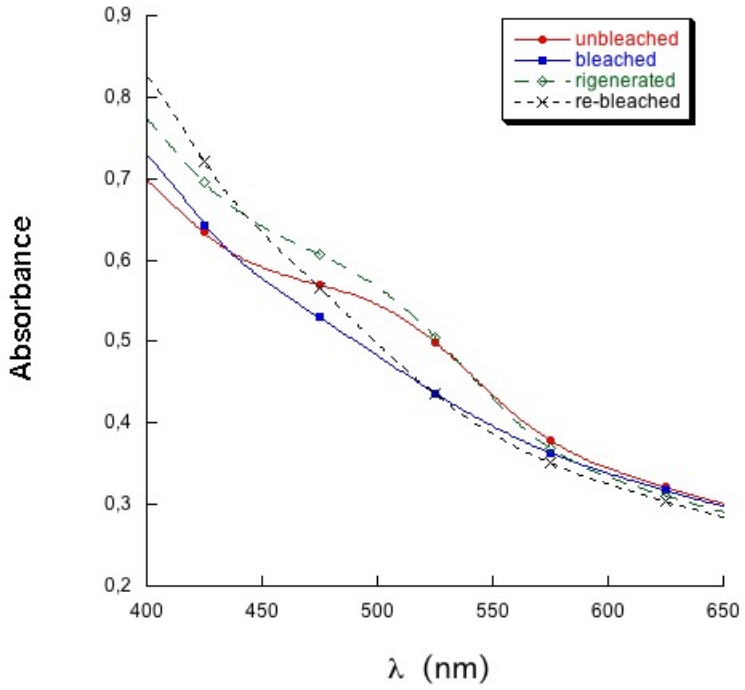

Figure 2.8: Absorption spectra of the same sample: before exposure to light (unbleached); totally bleached; after the addition of 11-cis-retinal (regenerated) and after another complete exposure to light (re-bleached).

after the regeneration of the chromophore. The vertical shift following regeneration, visible in the figure, is the consequence of the process of regeneration which causes a change of the suspension, leading to a shift of the vertical position of the spectrum but without influence on the absorption maximum [33].

Chapter 3

Electrophysiological responses of the mouse retina to ^{12}C irradiation

3.1 Do mice perceive light flashes?

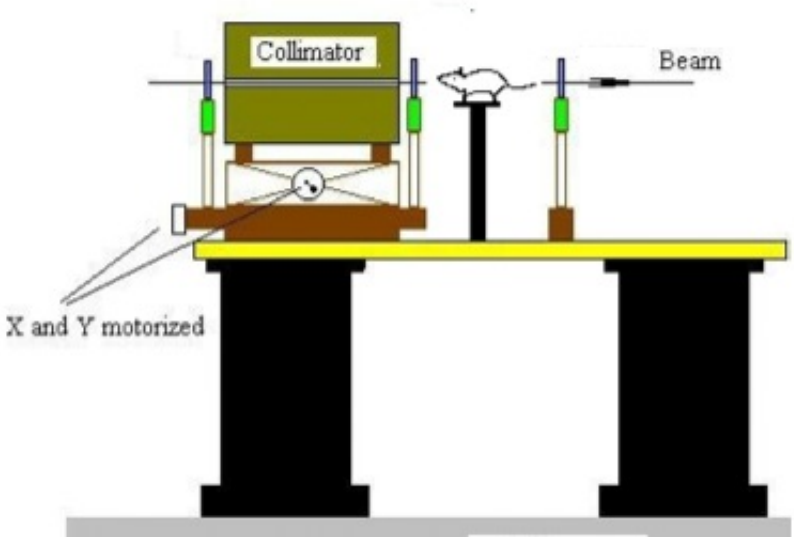

After the first LF reports, scientists programmed measurements in space, asking astronauts in the following Apollo missions to devote time for systematic observations of the phenomenon. Moreover, as mentioned in the preceding chapter, Several experiments in particle accelerators were performed concurrently with the space investigations. The experimenters received a minimal quantity of ionizing radiation in their eyes and psycho-physiological responses were recorded. These works were

published from 1970 to 1978. The particles explored have been μ, π, He, C, N and neutrons (see [9] and references therein). The beams were directed in different directions almost always towards the eye. Almost all were able to cause LF sensations in some configuration of the parameters. Only non-energetic neutrons ($3\,MeV$) and very energetic pions ($1.5\,GeV/c$) failed to produce LF at the chosen set of the parameters. In two cases the beams passed through the visual cortex (N at $266\,MeV/n$ and cosmic μ) and in both cases there was no LF perception. Detection thresholds were searched for in a few measurements: with μ and π at least $150-300$ particles in each burst were needed for LF perception. The two heavier ions (N and C) were used in single-few particle mode: N ($240\,MeV/n$, lateral incidence) 15 per burst, 40% efficiency; N ($531\,MeV/n$, 25° incidence), single, 10% efficiency; C ($470\,MeV/n$ and $595\,MeV/n$, 60° incidence), $1-2$ per burst, $10-67$% efficiency.

A possible classification of the output of these experiments, beside perceptions and rate of LF, concerns the LF shape. During the many controlled experiments there had been an effort to link LF characteristics with the possible processes that might have generated them. As an example, the diffuse LF, sometimes with dark center, appeared to be related to Cherenkov radiation. However, the very partial coverage of the parameter space did not allow for final associations.

As mentioned the ALTEA project proposes an animal *in vivo* model for the study of the origin of the radiation-induced phosphenes [2]. It is aimed at studying the electrophysiological dynamics of mice, while the eye or the visual cortex region is irradiated with very short bursts of heavy ions.

The principal objective of the ALTEA-MICE experiments is the investigation on the general mechanism responsible for originating the LF. In controlled conditions, in accelerator, the cosmic radiation of ionizing particle (^{12}C at $200\,MeV/n$) is simulated. About the use of the carbon ion ^{12}C, it could be useful to remember that in the primary cosmic ray spectrum heavy ions constitute only the 1% of the total amount of ions; among these heavy ions, the carbon ion is the most abundant. This happens also inside the ISS as is discernible in figure 1.3, where the preliminary data from ALTEA-DOSI are showed.

In the following we describe the ALTEA-MICE experiments: the kind of inci-

dent particles used; the experimental apparatus; the experimental sessions and the results. In particular, we report that ^{12}C ions activate the adult mouse retina and electrophysiological correlates of phosphenes can be studied *in vivo* [1].

3.2 Below Cherenkov radiation threshold

Cherenkov radiation [34] arises when a charged particle in a material medium moves faster than the speed of light in that same medium. The speed of light in the medium is given by

$$\beta\, c = v = \frac{c}{n} \tag{3.1}$$

where n is the refractive index and c is the speed of light in a vacuum, and β is the velocity in terms of the velocity of light. A particle emitting Cherenkov radiation must therefore have a velocity

$$v_{particle} > \frac{c}{n} \qquad or \qquad \beta_{particle} > \frac{1}{n} \tag{3.2}$$

For relativistic energies (and this is the case) the following expression for β has to be used

$$\beta = \frac{\sqrt{E^2 - M^2c^4}}{E} \tag{3.3}$$

with the total energy $E = E_{kin} + Mc^2$. Introducing the *specific energy*, $E_{spec} = E_{kin}/A$, for an ion of A nucleons, and replacing the total mass by the proton mass times the number of nucleons $M = m_p \cdot A$, we have

$$\beta = \frac{\sqrt{(E_{spec} + 935\,MeV)^2 - (935\,MeV)^2}}{E_{spec} + 935\,MeV} \tag{3.4}$$

it should be noted that the velocity depends only on the specific energy and is independent of the mass or atomic number of the ion. Because of the crucial importance of the projectile velocity in the energy loss calculations, this is a major reason for the use of specific energy instead of the total energy in radio-biology.

Since, for our purposes, liquid water can be considered a good approximation of biological target material, we insert the index of refraction of the liquid water $n = 1.333$ in the 3.2: we find out $\beta = 0.75$, that is $v_{particle}$ above 75% of the velocity of light in vacuum is requested to obtain Cherenkov radiation inside the target

medium. In general, inverting 3.4, we obtain the condition to Cherenkov radiation to arise, in terms of the specific energy

$$E_{spec} > \left(\frac{n}{\sqrt{n^2 - 1}} - 1 \right) \cdot 935 \, \frac{MeV}{n} \tag{3.5}$$

if we substitute $n = 1.333$, we obtain $E_{spec}^{threshold} = 478.6 \, MeV/n$. In all the measurements carried out at GSI laboratories carbon ions ^{12}C at $E_{spec} = 200 \, MeV/n$ were employed. Using 3.4 we obtain $\beta = 0.567$, that is nearly 57% of the velocity of light. These simple calculations ensure us that no Cherenkov emitted photons interfere with the mice vision systems during the irradiation sessions.

3.3 Experimental apparatus

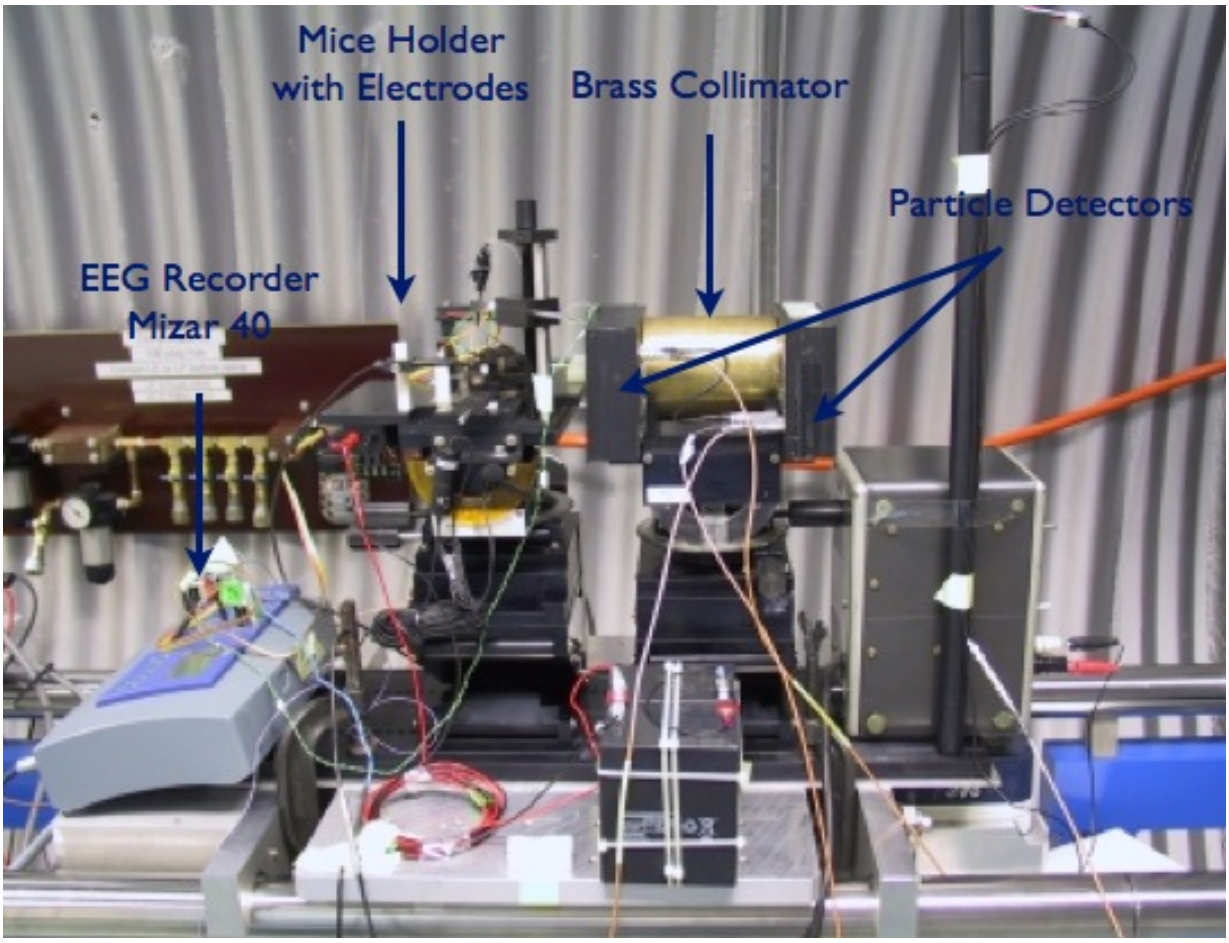

Figure 3.1: Mouse holder in the cave

A setup has been designed and built to hold the mouse and provide capability for remote controlled alignment to the beam (figure 3.1). The same setup permits the animal to be stimulated with light (with a white LED), to monitor the experiment with an infrared video camera, to precisely position the electrodes (cortical and retinal), to control the temperature of the animal, and to quickly change the animal maintaining the alignment set.

The irradiation took place in GSI *cave* A, while from the *control room* it was possible to send the light stimuli and to monitor the steps of the procedures. The whole measurement was remotely controlled from the beam line control room. In the *mice room* the mouse underwent anesthesia and the proper preparation before irradiation in a stereotaxic platform (the removable part of the holder) and was brought into the cave, see figure 3.2.

The electrophysiological signals have been recorded by a devoted EEG recorder (Mizar 40, EBNeuro). Six different channels have been used. Two of these (range $\pm 65\,mV$) were used to record the cortical and retinal signals respectively (with their references). Another channel has been devoted to the encoder, which convert the signal from two scintillator detectors: this channel records the counts of the particles through two detectors, one placed before the brass beam collimator and the other placed after the beam collimator to monitor the passage of the particles (see figure 3.1). A microphone output is connected to another dedicated channel of the EEG recorder to monitor possible auditory contamination.

In the offline analysis it is also possible to use as trigger signal both the 'start' of the visual stimulation (LED) or the 'start' of the beam of particles. For all the channels the acquisition frequency has been $1024\,Hz$. To avoid electrical noise, a $15\,V$ battery power has been used for the MIZAR 40 equipment.

An optical fiber connects the EEG recorder, situated in the cave, with a personal computer in the control room, where is possible a real time evaluation of the quality of the signals and the validity of the responses to the stimuli.

Two kinds of brass beam collimators have been used in different sessions: with holes of $5\,mm$ and $3\,mm$ of diameter.

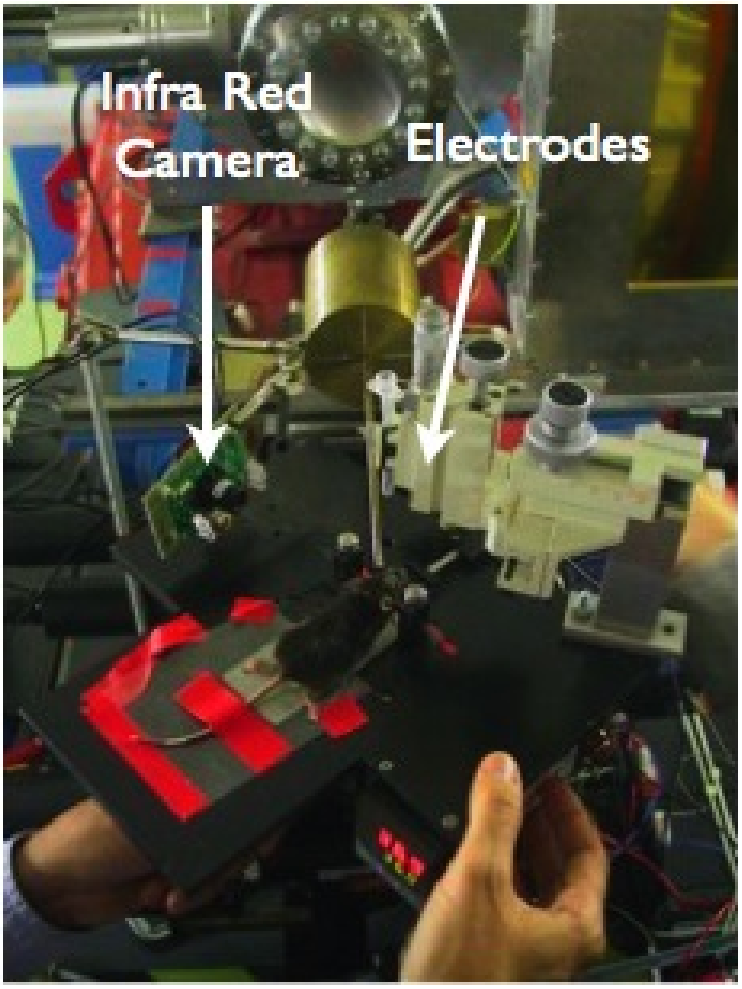

Figure 3.2: Detail of the stereotaxic platform of mouse holder

3.4 Experimental sessions

Three preliminary run sessions were performed at:

- GSI: ^{12}C, $100 - 300\,MeV/n$; pulses $5\,ms$ long; interval between consecutive pulses: $10 - 20\,s$; $1 - 2$, 500, 3000, 5000 part/burst.
- GSI: ^{12}C, $200\,MeV/n$; pulses $2\,ms$ long; interval between consecutive pulses: $2\,s$.
- BNL: ^{28}Si, $0.6\,GeV/n$; pulses $5\,ms$ long; interval between consecutive pulses: $20\,s$; 5000 part/burst.

These three preliminary sessions have been a useful test for the experimental apparatus and for improving the procedures.

After these preliminary sessions a subsequent session took place at GSI (2006). This session is considered is considered in the following [1]:

- GSI: ^{12}C, $200\,MeV/n$; pulses $2\,ms$ long; interval between consecutive pulses: $3\,s$; $10^3 \div 10^4$ particles/burst.

We exposed the eyes of 22 wild-type adult female mice (C57BL/6J; 89 weeks) to repeated bursts of ^{12}C ions and recorded electrophysiological signals from the retina and visual cortex. Under anesthesia by ketamine ($80\,mg/kg$) and xylazine ($16\,mg/kg$) and following pupil dilation (1% mydriacyl; 2.5% phenylephrine HCl), the mouse was positioned in the stereotaxic platform housing a heating unit to maintain the body temperature stable. The stereotaxic was then placed on the mouse holder platform at the end of the beam line where the beam was collimated to $3\,mm$ in diameter and directed approximately perpendicular to the posterior pole of the left eye. A coiled stainless steel wire making contact with the corneal surface through a 1% methylcellulose layer and referenced to the chin was used to record the electroretinogram (ERG); intradermal platinum needles placed over the visual cortex and referenced to non-visual locations recorded the cortical response (VEP). After completing the setup procedures, all lights were extinguished and the accelerator room evacuated. To check the overall system, light-evoked ERGs and VEPs

were recorded before (beginning after $\approx 20 - 30\,min$ dark adaptation) and at the end of irradiation. In these trials, the mouse was exposed to 100 full-field flashes of $1\,ms$ in duration delivered by a white LED at $1\,Hz$. Three to five hundred ^{12}C bursts were then delivered from the accelerator. To assume that the mouse visual system interprets each burst as a single-energy delivery, the burst length is kept below $2\,ms$. The right eye was not exposed to the direct beam irradiation. Retinal and cortical signals were recorded at $1024\,Hz$. The number of particles/ burst was measured online by one $5\,mm$ scintillator placed on the beam line in front of the mouse, with threshold set above background level.

After that the retinal and cortical signals data were analyzed and averaged offline after filtering out noise. Some results are shown in the following section.

3.5 Results

Light stimulation of the retina evoked replicable ERG and VEP responses in all mice before and after irradiation, although the response amplitudes varied among animals. For the sake of clarity, in figure3.3 a typical ERG signal is reported with some explanation on the nomenclature.

In figure 3.4 we show a comparison between the behavior in function of the time of the b-wave amplitude in retinal responses to light stimulations for mice exposed to radiation (with a total amount of dose of $\approx 50\,mGy$ and an amount of $10^{-4} \div 10^{-3}\,Gy$ per burst), and control mice (that is mice which were not exposed to radiation). The time (in seconds) in the abscissa is the duration of the experiment; the green circles belong to mice which underwent irradiation, while the black ones belong to control mice (that is not exposed to radiation). The amplitude of the b-wave near the origin of the axis is compatible among irradiated and control mice. In the following 20 minutes ($1200\,s$), after the first exposition to the LED pulses, all the mice remain in dark condition, but some of them (indicated by green color) underwent some burst of radiation, absorbing $\approx 50\,mGy$, while the other weren't irradiated at all. After this interval of time the b-wave amplitudes of the two groups of mice are compatible again, that is that the increased amplitude (increased by

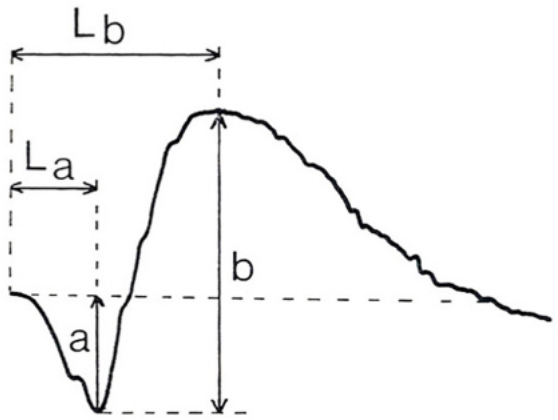

Figure 3.3: ERG parameters which are customarily measured. The size of the a-wave is measured from the baseline to the trough of the wave. The size of the b-wave is measured from the trough of the a-wave to the peak of the b-wave. The time-to peak from both waves (L_a and L_b) is determined from stimulus onset to the trough or peak of the waves.

almost a factor two with respect the amplitude in the origin) is compatible with the physiological elongation of the b-wave amplitude due to a major time of dark adaptation. Thus the functionality of the response seems not to be affected at short times by the absorbed dose.

Retinal responses to ^{12}C ions were obtained in 11 of 22 mice tested in the described session; the proportion of positive trials is consistent with the percentage ($\approx 20 - 50\%$) of heavy nuclei found to be successful at phosphene induction in human studies mentioned before. This variability may reflect physical phenomena that are known to occur when ionizing particles impact living tissues (e.g. direct ionization due to energy released by crossing heavy nuclei, indirect effects in a knock-on process involving protons, neutrons, etc.) or physiological differences between mice. Effects of the energy locally supplemented by the heat on the cone/rod systems contributing to the response may also account for this variability [1].

In figure 3.5 the retinal and cortical responses are plotted. The grand average is represented by a continuos line, while the standard error is indicated by the halo around the line. The vertical bars indicate the start of the stimulations: light stimuli

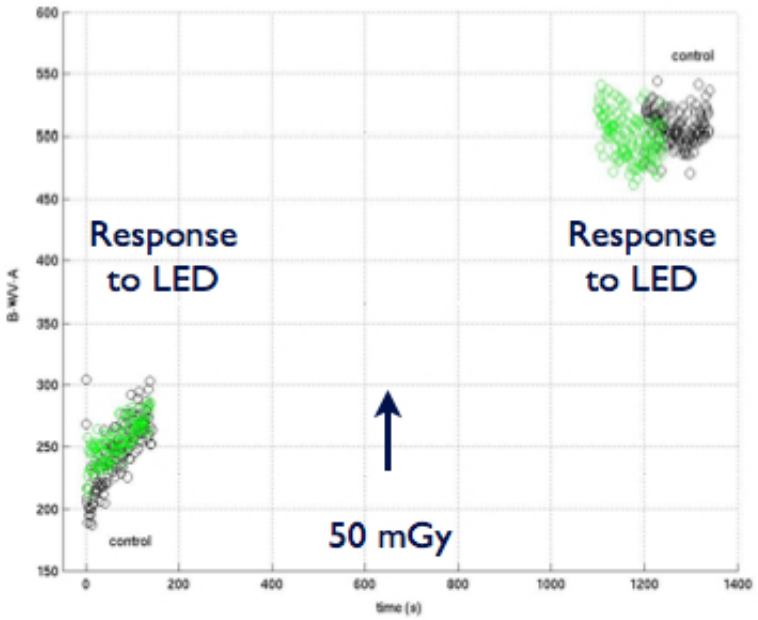

Figure 3.4: From preliminary sessions data. Comparison of the b-wave amplitude in retinal responses to light stimulations for mice exposed to radiation (green) and control mice (black). In abscissa there is the absolute time (s).

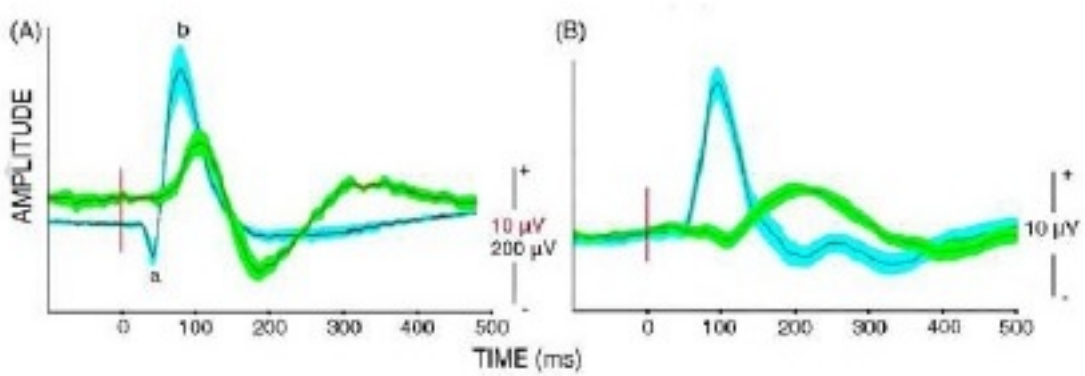

Figure 3.5: Grand average and standard error of retinal (A) and cortical (B) responses to light (black/light-blue) or bursts of ^{12}C ions (black/green). Vertical bars indicate light stimuli or the beginning of ^{12}C ion bursts. Waves a and b of light-evoked ERG are indicated (from [1]).

furnished by the LED pulses or the impinging bursts of particles. From this figure we can observe a main positive wave, significantly smaller in amplitude than the b-wave of light-evoked ERG and with longer latency ($\approx$ 28% mean increase), characterized all retinal responses to ^{12}C ions; this significant positive wave is preceded by a distinct early negative wave only in some animals.

Cortical responses suggesting activation of the visual pathways were always associated to the retinal response to ^{12}C ions (with lower amplitude - about 1/3 - and longer latencies - $\approx$125% mean increase - than the light-evoked VEPs) and never observed in the absence of particles irradiation (figure 3.5 B).

In figure 3.6 we compare the feature of the bursts of particle to the b-wave amplitude of the retinal signals of the only mouse we have been able to measure responses to single burst. The threshold ion intensity evoking a recognizable retinal response was approximately 1000 ions/burst (0.36 mGy/burst). The response amplitude increased sharply (and apparently linearly) above this level to a maximum at approximately 2000 ions/burst (0.72 mGy/burst)

This mouse was excluded from the average of the figure 3.5, because of its very surprising response to the ^{12}C irradiation stimulation. In figure 3.7 the recorded real time retinal responses of this mouse to the bursts of carbon ions is reported. As mentioned the retinal response in figure 3.7 is large enough to allow identification of single responses without signal averaging and provides significant, although anecdotal, information. In this mouse, the response waveform was comparable to the light-evoked ERG, with recognizable components similar to the a- and b-waves.

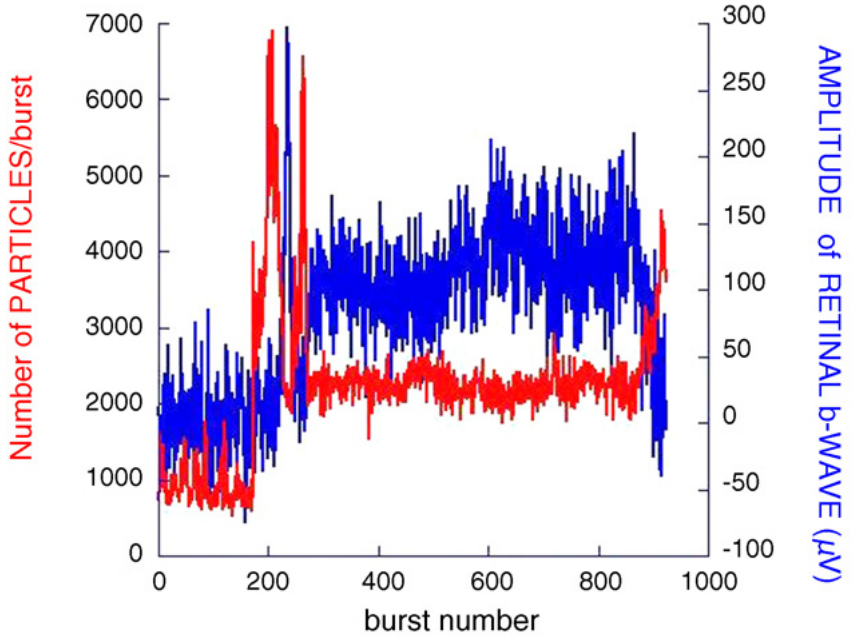

Figure 3.6: Amplitude of the main positive wave of the mouse shown in figure3.7 (blue) and number of ^{12}C ions per burst (red) over repeated ^{12}C ion bursts.

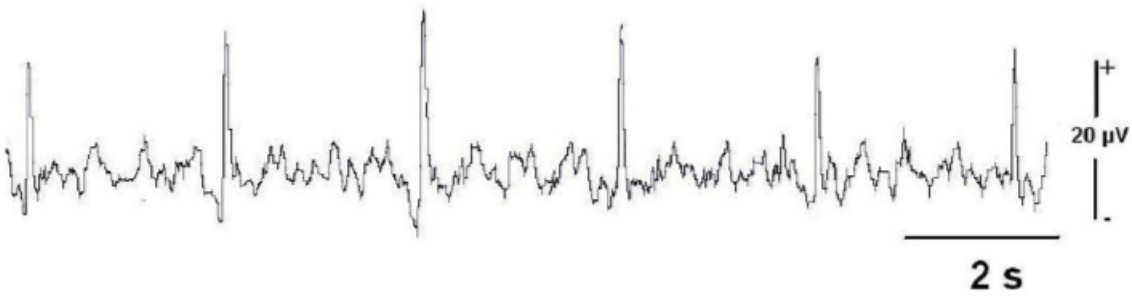

Figure 3.7: Raw data from mouse with large-amplitude retinal responses.

Chapter 4

Radiation effects in the ALTEA-biophys experiments

Ionizing radiation interacts with matter, producing physical, chemical, and biological consequences. Actually the designation "ionizing" is restrictive because the process of ionization refers specifically to the ejection of an electron from an atom or molecule thereby creating a ion-pair. Ionizing radiation may activate physical and chemical effects in matter including heat generation, atomic displacements, electronic excitation of atoms and molecules, breaking of chemical bonds and nuclear reaction. The specific effects depend on the type of radiation, the target, and the irradiation conditions.

The physical properties of heavy ions determine in some extent their biological action; the quantitative interpretation of biological effects requires a knowledge of the spatial distribution of energy deposited within tracks, commonly referred to as track structure. The interactions of ionizing radiation with matter always take place at the level of individual atoms. Except for nuclear reactions, the energy scale is many orders of magnitude smaller than the kinetic energy of an ionizing entity. Accordingly, a single interaction between a ionizing particle and the matter can initiate a multiplicity of effects.

In this chapter the physical behavior of diffusion and energy delivery of charged ion particles through the biological sample are reported. In particular the role of carbon ions is underlined, because of its importance in our experiments related to

ALTEA-biophys and *ALTEA-MICE*.

After a brief description of the mechanism of the energy delivery and the track structure, a model based on classical collision dynamics is showed. The chapter also includes the description and explanation of our experimental data obtained irradiating, in controlled conditions, samples of intact bovine rod outer segments in suspension.

According to [36], here we classify ionizing radiations in a medium as of low, intermediate, or high linear energy transfer depending on the linear energy transfer[1] (LET) value falling below 10^{-1}, lying between 10^{-1} and 10, or exceeding $10\,eV/\mathring{A}$ ($1\,eV/\mathring{A} = 10\,keV/\mu m$). Moreover the spatial patterns of energy deposition are divided into two classes of *sparsely* ionizing ones such as electron, x- or γ- rays, H^+ tracks and *densely* ionizing tracks such as heavy ions, that is from He^{+2} on.

In the experiments we carried out at GSI laboratories ^{12}C ions at $200\,MeV/n$ were used, with an intermediate LET of $\approx 17.4\,keV/\mu m$.

4.1 Effects of heavy ion interaction with matter

Ions interact with matter by three processes, depending on their energy

1. electron capture (low energies)
2. collisions with atomic electrons (medium and high energies)
3. nuclear collisions and nuclear reactions (very high energies)

The particle velocity is the main parameter governing the stopping processes and determines, first, the charge state of the projectile, and, second, the type of interaction mechanism between the projectile and the target. If the velocity of the projectile is greater than the orbital velocity of its own electrons, then the electrons of the projectiles will be stripped off by the interaction with the target material [2].

[1] For the definition of the linear energy transfer see section 4.2.

[2] The orbital velocity in the Bohr model is given by $v = \alpha Z \times c/n$, with $\alpha = e^2/hc = 1/137$. Z is the atomic number and n is the main quantum number.

The effective charge as a function of energy is frequently approximated by the semi-empirical Barkas formula

$$Z_{eff} = Z\{1 - exp(-125\beta Z^{-2/3})\} \tag{4.1}$$

The effective charges Z_{eff} are used for LET calculations and is valid for condensed targets. For high energies - as for the ^{12}C ions at $200\,MeV/n$ -, all electrons are stripped off the projectile and the effective charge equals the atomic number.

The stopping power gives the energy loss rate of the incident particle: the deposited energy appear in the molecules of the medium, at first in electronic form [36]. On energy absorption form the impinging particle, a molecule is raised to one of its spin-allowed (singlet S) excited states. If the excitation energy exceed the ionization potential, the minimum energy required for electron ejection, ionization may occur. In principle, spin-forbidden (triplet T) states may be excited by the impact of slow electrons - a shower of low electron is expected for any incident high-energy radiation. If produced, these triplet states eventually decay to the ground state. In almost all theories of aqueous radiation chemistry, the primary species are assumed to be formed from singlet (excited or ionized) states.

Excited states of a *typical organic molecule* can undergo various transformations as follows:

- Internal conversion - that is, without change of multiplicity - to the lowest singlet, or to the ground state ($S_n \rightarrow S_1$ or S_0)
- Fluorescence, including delayed fluorescence ($S_1 \rightarrow S_0 + h\nu$)
- Intersystem crossing - that is, with a change in multiplicity ($S_1 \rightarrow T_1$ or $T_1 \rightarrow S_0$)
- Phosphorescence ($T_1 \rightarrow S_0 + h\nu$)

In *condensed media* we must add to this list *energy transfer process*. These are broadly classified as

- Coulombic processes
- Electron-exchange processes

In the radiative coulombic process a real photon is emitted by the donor molecule D, and the same is absorbed by the acceptor molecule A. The effectiveness of this process depends on, among other factor, the degree of overlap between the emission spectrum of the donor and the absorption spectrum of the acceptor. In this kind of interaction, the dipole-dipole term dominates over higher-order dipole terms. Theories of energy transfer mediated by dipole-dipole interaction gives a rate varying inversely as the sixth power of donor-acceptor distance. This transfer extends over relatively long distances (some nm) and is in competition with deactivation of D^* (internal conversion and/or intersystem crossing).

In contrast, the electron-exchange interaction is short ranged; its rate decrease exponentially with the donor-acceptor distance; this is expected since, for the electron exchange between D^* and A, respective orbital overlap would be needed.

The major part of the energy dissipation of a heavy particle is due to the interaction with the target electron. Actually, in general, also the nuclear stopping contributes. Compared to electronic stopping, nuclear stopping is due to different reaction mechanism. In the electronic stopping process, single electrons are ejected from bio-molecules, but this does not necessarily lead to a destruction of the chemical binding and to the disintegration of the molecule. Missing electrons can be restituted before the chemical bonds are broken. In nuclear stopping processes the projectiles interact with the complete target atom and the target atom will be kicked out of the chemical surrounding if enough energy is transferred.

4.2 Energy loss: stopping power and LET

Energy transfer from a charged particle can be considered from two points of view: (1) the *particle* - that is, its charge, range, penetration, etc.; or (2) the *matter* - receiving the energy to produce chemical changes, charge separation, luminescence, et cetera.

The stopping power of a medium toward penetrating charged particle is the *energy loss suffered by that particle per unit path length*, whereas the *linear energy transfer* (LET) refers to the energy *received by the medium* in the immediate vicinity

of the particle track. Their difference arises because, even at the shortest time, significant amounts of energy may be removed from the track vicinity. So LET is the amount of *locally* absorbed energy per unit length, which leads to ionizations and/or excitations within the considered site. The remaining kinetic energy of particles leaving the site is excluded.

It has become customary [35] to specify a limit of energy deposition below which the deposition is considered to be local (*energy restriction*); $100\,eV$ has been widely accepted. The energy limits are also called "cut-off energies", their values in eV are indicated by subscripts to LET (e. g. LET_{200}). The *total transferred energy* per unit length (the *stopping power*) $-dE/dx$, is numerically equal to LET_∞, i.e. without restriction.

Dose D is the common exposure parameter in radio-biology; in the International System of Units it is measured in $J\,kg^{-1}$ with the special unit gray (Gy). The dose deposited by particles in a target is determined by the number of traversing particles and linear energy transfer of each particle. If the dimensions of a biological target are larger than the diameter of the individual tracks and if no restrictions on the energy transfer, whether coming from high- or low- energy electrons are applied, then the LET is identical with the total energy loss dE/dx of the heavy charged particle. The dose can be calculated using the formula

$$D[Gy] = 1.6 \times 10^{-9} \times LET\left[\frac{keV}{\mu m}\right] \times \Phi\left[\frac{part}{cm^2}\right] \times \frac{1}{\rho}\left[\frac{cm^3}{g}\right] \tag{4.2}$$

where $LET = dE/dx$ is the linear energy transfer without limitation, LET_∞, [35] and equal to the energy loss dE/dx; Φ is the particle fluence; and ρ is the density of the stopping material, i. e. $1\,g/cm^2$ for water.

This expression can be used for track segment experiments, in which the LET does not change significantly during the passage of the particle through the biological target. For ions of low specific energies of a few MeV/n, the variation of LET is very large and therefore only very thin biological targets like cells in mono-layer or thin DNA films can be used. For high-energy ions of several $100\,MeV/n$, track segment conditions can be realized even for an extended target.

In order to compare the different biological response of ions relative to conventional x-ray irradiation, the *relative biological efficiency* - RBE - is defined as the

ratio of x-ray dose versus the dose delivered by ions required to achieve the same biological effect

$$RBE = \frac{D_x}{D_{ion}} \tag{4.3}$$

with D_x and D_{ion} being the X-ray and ion doses, respectively. It's of particular importance to realize that the RBE depends on numerous physical and biological parameters such as ion species, ion energy and dose as well as the biological endpoint and the tissue type under consideration.

In the experiments carried out at GSI laboratories ^{12}C ions at $200\,MeV/n$ were used. In figure 4.1 the energy loss as a function of penetration path is depicted; the data and the plot have been carried out by 'The Stopping and Range of Ions in Matter', SRIM program, which calculates the stopping and range of ions - ion particles with energies from $10\,GeV/n$ up to $2\,GeV/n$ - into matter using a quantum mechanical treatment of ion-atom collisions. The SRIM simulation mimic the irra-

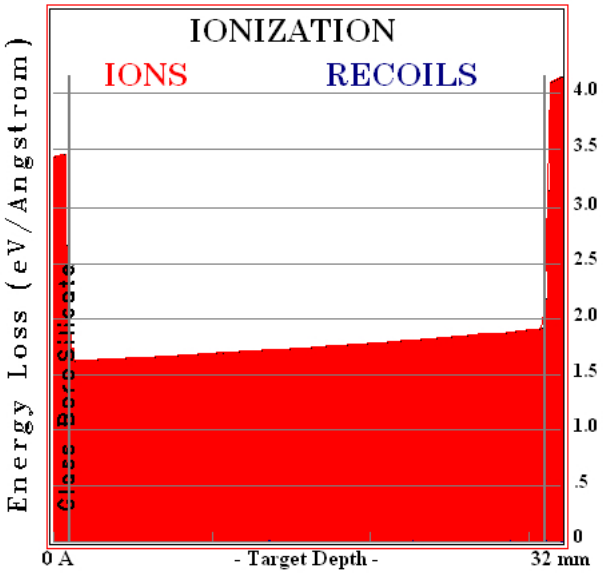

Figure 4.1: Plot of SRIM data output simulation (3000 events). The projectile is ^{12}C ion at $200\,MeV/n$, while the target is composed of three layers: two glass surfaces ($1\,mm$ thick each), and a $3\,cm$ layer of liquid water, arranged as in figure.

diated biological samples contained in a glass vial $3\,cm$ long in the direction of the ^{12}C ion burst. For our purpose liquid neutral water is used to simulate biological

compounds, whereas two $1\,mm$ layers of boron silicate glass (available in the SRIM table of compounds) were used to reproduce the vial.

From the SRIM data output simulation showed in figure 4.1 we get the average value of the LET in water, $LET_{average} = 17.4\,keV/\mu m$, while the maximum and minimum values in water are respectively $LET_{MAX} = 19.0\,keV/\mu m$ and $LET_{MIN} = 16.1\,keV/\mu m$. Because the variation between LET_{MAX} and LET_{MIN} is $\approx 3\,keV/\mu m$, so the LET doesn't change significantly through the target, and we assume the track segment conditions were realized. So we can consider the LET in our experimental condition the same as in water, as typical biological medium, $LET_{water} = (17.4 \pm 1.6)\,keV/\mu m$, where the error is assumed to be $\Delta LET = max\{(LET_{average} - LET_{MIN}), (LET_{MAX} - LET_{average})\}$. This value for LET_{water} will be used forward in our calculations and discussions.

The major part of the energy dissipation of a heavy particle is due to the interaction with the target electron. For the sake of completeness, we observe [37] that the nuclear stopping contributes only a small part to the total stopping process at medium or high energies but plays a significant role at low energies ($E \leq 10\,keV/\mu m$) at the very end of the particle track. So, from figure 4.1, and correspondent simulation data, we can assume the nuclear stopping can be neglected in our analysis.

4.3 Electron emission

The macroscopic dose of a particle beam is given by the number of particles traversing the mass unit and the dose deposited by each particle. According to the Bethe-Bloch-formula the energy is transferred to the target electrons that are emitted as δ-electrons[3] (high-energy δ-electrons can form individual short tracks, called δ-rays).

There are several processes that contribute to the features and the spectrum of

[3]The term δ-electron is frequently used with different meaning in radio-biology and in atomic physics. In atomic physics, δ-electrons are all electrons of the continuos spectrum. In radio-biology the term δ-electron is used to differentiate the high energetic electrons from to low energetic electron, which are called simply electrons. Here the terminology of atomic physics will be used, calling all electrons of the continuous electron spectra δ-electrons.

the emitted electrons. For a high-energy transfer, the binding energy of the electrons can be neglected and electrons are treated as a free electron gas undergoing binary collisions. These electrons are emitted in radial symmetry around the centre of mass system that coincides with projectile system, because of the large mass excess of projectiles compared to electrons. The main characteristic of these emission processes is shown in a velocity plot in figure 4.2 A e B. At lower energy transfer,

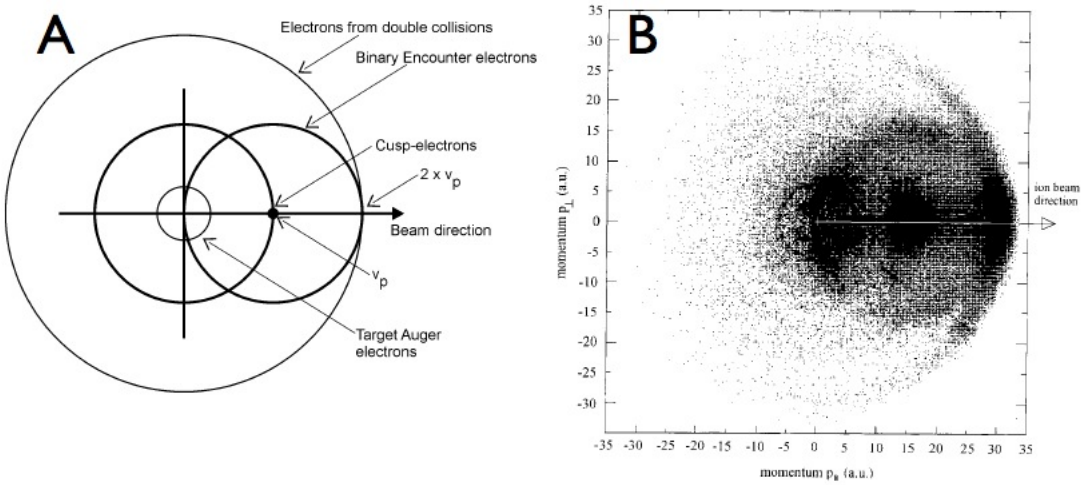

Figure 4.2: (A) Velocity coordinates of the electron emission in ion-atom collisions. (B) Angular distribution of the measured electron emission. From [38].

the binding to the target atom becomes more relevant and the collision has to be calculated as a three-body interaction yielding a large number of electrons emitted with low velocity. At low particle energies, weakly bound electrons are exchanged with the target yielding a high-intensity peak at the velocity of projectile. These are called cusp electrons, due to the characteristic line-shape of their energy distribution. At higher energies this peak disappears because no electron can jump into bound states. Finally, due to the collision process, vacancies in inner atomic shells can be produced in both atoms, target and projectile; when these vacancies are filled by outer electrons, the difference in the binding energies can be emitted either as photons or as kinetic energy of electrons if the energy is larger than the ionization energy: these electrons called Auger electrons have a discrete energy and are emitted from both target and projectile atoms.

The main characteristic of these emission processes is shown in a velocity plot

in figure 4.2B. Most of electrons are emitted in a forward direction.

For the calculation of the radial dose distribution around the particle track, the transport and energy deposition of these electrons has to be followed through the target material. The transport is characterized by elastic and inelastic scattering. While the elastic scattering changes only the direction, the inelastic processes - ionization and excitation - can cause further biological damage.

4.4 The role of the track structure: track core and track halo

The physical properties of heavy ions determine in some extent their biological action; the quantitative interpretation of biological effects requires a knowledge of the spatial distribution of energy deposited within tracks, commonly referred to as track structure.

Heavy charged particles interact mainly with the electrons of atoms and molecules. The liberated electrons may possess sufficient energies to travel considerable distances from their point of origin in the paths centre. The track is hence by no means a straight line and looks rather like a "test tube brush" (R Katz). A charged particle (*e.g.*, proton, deuteron, alpha) loses kinetic energy via a sequence of small energy transfers to atomic electrons in the medium. The incident particle has a fixed momentum before any interaction with the atoms of the mean; its momentum after exciting some atoms into some excited sates is modified. We can say the wavefunction of the system before any interaction is the uncoupled product of the wavefunctions of the atom and the incident particle. After the first interaction, these wavefunctions get inextricably mixed, and each subsequent interaction makes it worse.

A *track* is generated by energy loss correlated events along the direction of the momentum of the penetrating particle. Most of the energy deposition occurs in the infra-track, a narrow region around the particle track extending about 10 atomic distances. Ionization outside the infra-track is caused by very energetic particles that escape from the infra-track and secondary electrons (see figure 4.3). The more

energetic interactions eject electrons from their parent atoms and generate primary ion-pairs. Since only a small fraction of the initial energy is transferred at each

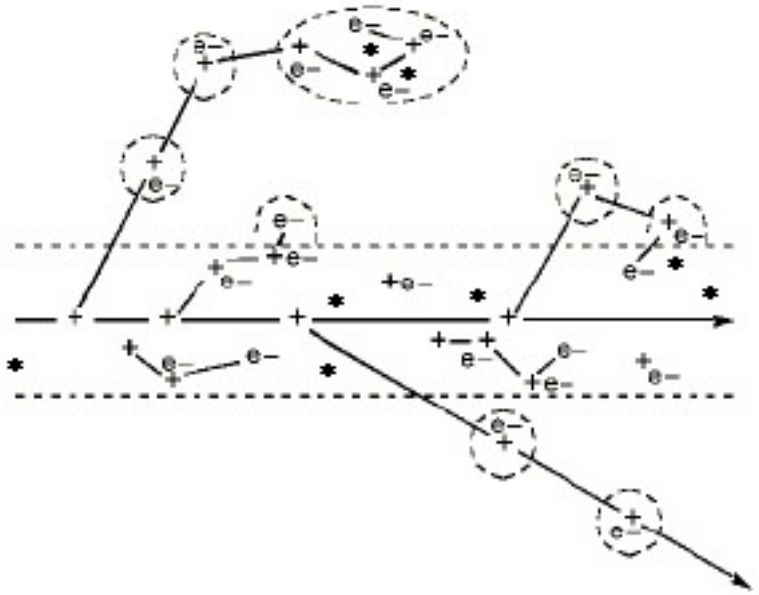

Figure 4.3: Heavy ion track structure, secondary electrons produced by more energetic interactions.

event, a track consisting of clusters of ions or spurs is generated along the path of the moving particle. Most spurs in water comprise 1-5 ion-pairs.

Charged particle tracks in liquids are a little bit similar to cloud chamber tracks. In detail, there are great differences in track lifetime and possibility to observe the tracks. Tracks in the radiation chemistry of condensed media are extremely short-lived and are not amenable of direct observation.

In our description [39] the track is subdivided into a *core*, characterized by a high-energy density region, and a *penumbra*, characterized by a low-energy region which is operationally helpful but should not be taken to suggest that the interaction mechanisms are different. Figure 4.4 illustrates the track structure in a very schematic way. The ions collide with atomic electrons which are liberated with different starting energies and ejection angles depending on the ions speed.

The track halo (or penumbra) is formed by the electrons emerging from the projectile interaction area and dissipating their energy outside this area. The main

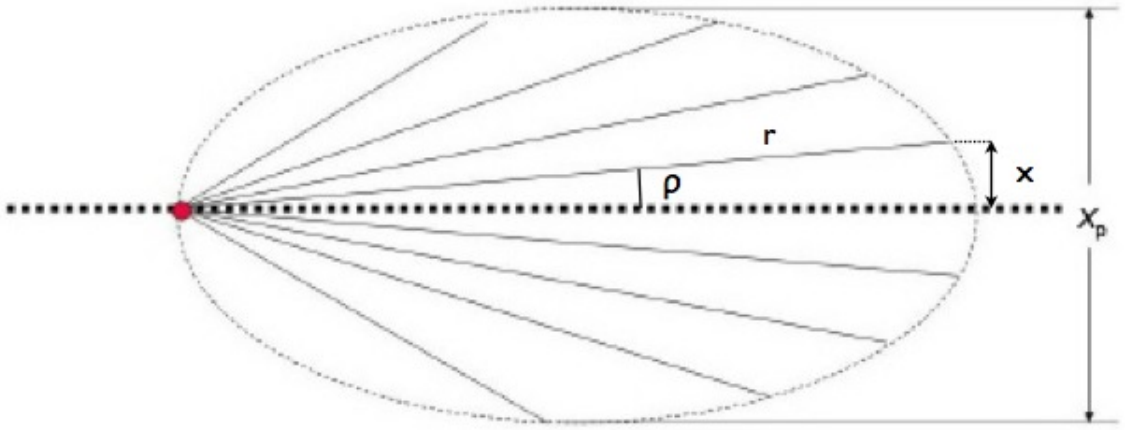

Figure 4.4: A schematic track structure model. The ion path is shown as a heavy dotted line. Electrons (light lines) are ejected at different energies and directions. The maximum radial extension, the penumbra radius x_p, is governed by the relationship between electron energy (and range) and ejection angle. From [39]

interactions of these electrons with target atoms are elastic collisions in which only the direction of the electrons changes and inelastic collisions in which energy of the electron is spent for either target excitation or ionization of target molecules. The dominant process, the ionization of the target molecules, is the major factor in the radiation damage of biomolecules. In the excitation process mostly small amounts of energy ($E \leq 10\,eV$) are transferred that are not sufficient to produce chemical changes.

The radial extension of the spatial distribution of energy deposited within tracks is particularly critical with very heavy and energetic ions, since they may deposit high amounts of energy even at comparatively large distances from the track centre due to the high density of far-ranging δ-electrons. The behavior is illustrated in the next subsection by using the model of Kiefer and Straaten [41].

A model based on classical collision dynamics

This model [41] provides the energy deposition in an ion track as a function of radial distance, on the basis of classical collision dynamics and using empirical range-energy

relationship for electron. In other words we can obtain information on the track structure, where by track structure is meant the distribution of energy loss events and their geometrical disposition.

The model is based on classical calculations of relativistic collisions between two point masses, the ions, possibly with relativistic velocity, and the electron initially at rest [35]. In spite of this simplified approach, measurements in simulated microscopic detectors showed that there are no large differences between the theory and the experiments [41]. We want to emphasize that in the simplifying assumptions made the electrons are supposed to be unbound so that interaction processes can be treated using collision dynamics. This will be particularly important for small electron energies and contributes to the fact that the model does not fit the experimental data at low specific ion energies.

A schematic representation of angular distributions and ranges of electrons liberated by ion impact is depicted in figure 4.4. Let ϵ_0 be the starting energy - after the collision - of the electron, ϵ_m the maximum value of ϵ_0 and ρ the angle between the directions of the ion and electron flight. And let x_0 the maximum distance perpendicular to the ion direction which the electron can travel. The penumbra radius x_p is the maximum of x_0 which can be found varying ϵ_0. In the case $\epsilon_m \ll 2\,m_e\,c^2$ this leads to the numerical expression of the penumbra radius for water as the absorbing medium [41]

$$x_p = 6.16 \cdot 10^{-2}\,(E_{spec})^{1.7} \tag{4.4}$$

where x_p is measured in micrometers (μm) and depends only on ion speed or specific energy $E_{spec} = E_{kin}/A$ - being A the nucleons of the ion - given in MeV/n.

For a given ion, LET increases with decreasing velocity[4] and hence also decreasing penumbra radius: the track becomes 'thinner'. Larger LET means then smaller tracks and hence smaller action cross sections which leads to the unexpected finding

[4] LET_∞ is given by the Bethe-Bloch formula: $-\frac{dE}{dx} = \frac{4\pi N z_m Z^2 e^4}{m_e v^2}\left[ln\frac{2m_e v^2}{I[1-\beta^2]} - \beta^2\right]$, where: N is the number of atoms of the mean per cm^3; z_m is the atomic number of the mean; v is the velocity of the incident particle and I is the ionization potential of the mean. For ^{12}C ions up to $400\,MeV$ the Bethe-Bloch formula becomes: $-\frac{dE}{dx} = \frac{4\pi N z_m Z_{eff}^2 e^4}{m_e v^2}\,ln\frac{2m_e v^2}{I}$

that the cross-section decreases with increasing LET. This feature has been termed 'thin out'.

The energy deposited in the track varies with radial distance from the track centre and reaches zero at the penumbra radius. The model also provides the energy density, i. e. the deposited energy per unit mass, given in Gy, as a function of radial distance x measured in μm in water

$$\rho_e(x) = 1.25 \cdot 10^{-4} \frac{Z_{eff}^2}{\beta^2} \cdot \frac{1}{x^2} \tag{4.5}$$

here Z_{eff} is the ion's effective charge defined in 4.1; β is the ion velocity relative to that of light in vacuo and x the radial distance from the track centre measured in μm. We can see that the energy density follows an $1/x^2$ dependence according to experimental measurements, see [41] and references therein. This behavior of the energy density as well as the the maximum radius x_p (called r_{max} in the following subsection) will be used in the local effect model (LEM) description.

Local effect model - LEM

Thus the radial dose deposition around the ion track is known to be essential for an assessment of radiobiological effects and for an effective consideration of physical and chemical damages induced by ion irradiation. We focus on the ionization density around the centre of ion tracks and subsequent chemical processes. Track structure models based on simple analytical formulae as well as radial dose distributions derived by means of Montecarlo simulations are used as input for the local effect model (LEM) [42], in order to calculate cell inactivation probabilities.

We denote the primary energy distribution generated by the physical processes of target ionization and excitation on a timescale of $10^{-15}\,s$ with *initial dose distribution*. The subsequent chemical processes such as radical diffusion within the target medium are additionally taken into account for the calculation of the *actual dose distribution* or track structure. The track structure calculations are based on considerations by Kiefer and Chatterjee [41]. All of them assume water as the relevant target and exploit the experimental results of gas chamber measurements that show a $1/r^2$-dependence of the initial dose distribution, if r describes the radial

distance from the track centre. Although these experiments are not performed for liquid water or in tissue, one can well assume that this dependence also holds for the cell environment.

The initial dose distribution used in the LEM [42] assumes that the track consists of an inner part (for $r < r_{min}$) with a constant initial dose attached to an outer part following a $1/r^2$-dependence. It can be expressed by

$$\mathrm{D(r)} = \begin{cases} \lambda\, LET/r_{min}^2, & r < r_{min}, \\ \lambda\, LET/r^2, & r_{min} \le r \le r_{max}, \\ 0, & r > r_{max} \end{cases} \tag{4.6}$$

where the maximum radius r_{max} corresponds to the x_p value expressed in 4.4, and λ is the normalization constant to assure that the radial integral reproduces the LET for a medium with density ρ

$$\lambda = \frac{1}{\pi\, \rho\, [1 + 2\, ln(r_{max}/r_{min})]} \tag{4.7}$$

The maximum radius r_{max} is determined by those δ-electrons with the highest energy. It was found [41] that r_{max} only depends on the energy E (in MeV/n) and, if the particle energy is above $1\, MeV/n$, can be parameterized by

$$r_{max} = 6.16 \cdot 10^{-2}\, (E_{spec})^{1.7} \tag{4.8}$$

with r_{max} in μm and E in $MeV/\mu m$, as already mentioned in equation 4.4.

The minimum or core radius r_{min} is $r_{min} = 10\, nm$ for the original model, the 'large' value of the radius to implicitly account for radical diffusion.

Actually in the model the track core radius is energy-dependent ([36], [44]) following this simple parametrization for the velocity dependent radius r_{min} of the inner part of the track

$$r_{min}(\beta_{ion}) = \beta_{ion} \cdot r_c \tag{4.9}$$

with $\beta_{ion} = v/c$, where v is the velocity of the particle, c is the speed of of light and r_c describes the larger extension of the inner part of the track. In this description the constant core dose D_c and the penumbra dose D_p as a function of track radius, r in μm, are given as follows

$$D_p(r) = 1.25 \cdot 10^{-4} \left(\frac{z_{eff}}{\beta_{ion}}\right)^2 \frac{1}{r^2} \equiv K_p \frac{1}{r^2} \quad [Gy], \tag{4.10}$$

$$D_c = \frac{1}{\pi r_{min}^2}\left(\frac{LET}{\rho} - 2\pi K_p \, ln\left(\frac{r_{max}}{r_{min}}\right)\right) \quad [Gy] \tag{4.11}$$

where as usual z_{eff} is defined in 4.1. The dose dependence in the penumbra expressed by equation 4.10 is determined by the classical collision dynamics. The constant core dose in equation 4.11 is normalized such that the radial integral of equations 4.10 and 4.11 yields the linear energy transfer. The core radius required to determine r_{min} was chosen to be $r_c = 11.6\,nm$.

Following the short physical stage ($< 10^{-15}\,s$), chemical processes start, where radicals that were created by interaction with primary ions or secondary electrons diffuse through the medium. They finally react with each other or with molecules in the irradiated medium such as sensitive sites of the DNA molecule. The radical diffusion length depends on the scavenging capacity and was determined to be $\sigma \approx 4\,nm$ for mammalian cells [45].

4.5 Radiation chemistry of water

Radiation chemistry deals with chemical reactions caused by *ionizing radiation*. One important difference to photochemistry lies in the fact that absorption is is not selectively restricted to special molecules, the *chromophores*, but involves the whole reaction mixture. The second point is that secondary particles are formed which ionize further molecules on their way (indirect effect). Thus interaction involves not a single type of absorbing species as in photochemistry but rather the system as a whole.

The number of altered molecules is related to the total absorbed energy. The respective quantity is termed *G value* and is defined as the number of altered entities (molecules or atoms, etc.) per $100\,eV$ absorbed energy

$$G = \frac{number\ of\ altered\ entities}{100\,eV} \tag{4.12}$$

It may also be expressed as *molar concentration per unit dose*. If $c\,(mol\,dm^{-3})$ is the concentration, $D(Gy)$ the dose and $\rho(kg\,dm^{-3})$ the density of the medium, the

following relation holds true

$$G = 9.64 \cdot 10^6 \, \frac{c}{D \cdot \rho} \tag{4.13}$$

If there are no chain reaction, G value below 10 are usually found. Doses around $10^3\, Gy$ are required to yield millimolar concentrations. This is outside the "physiological" range of most biological systems surpassing, e. g. "mean lethal doses" of mammalian cells by almost three orders of magnitude. Actually, following [36], we must remember that $G(X)$ indicates the $100\, eV$ *observed* yield for the species X.

As pointed out before, interaction with ionizing radiation does not only lead to localized ionizations and excitations but also to the liberation of secondary particles. The spatial distribution of energy deposition and hence reaction products can be extremely heterogeneous influencing speed and direction of secondary reactions. With sparsely ionizing radiations, the species formed in "spurs" and "blobs" will react each other before they are able to escape by diffusion. Water is the main constituent of living systems. In somatic and vegetative cells its fraction lies between 40% and 70%. Thus, most of the energy of ionizing radiation is absorbed by water molecules which are either excited or ionized

$$H_2O \quad (+h\nu) \quad \longrightarrow \quad H_2O^+ + e^-_{aq} \qquad \text{ionization} \tag{4.14}$$

Excitation of a water molecules is often followed by splitting of the molecule

$$H_2O \quad (+h\nu) \quad \longrightarrow \quad H_2O^* \quad \longrightarrow \quad H^\bullet + {}^\bullet OH \qquad \text{splitting} \tag{4.15}$$

The primary products are $H^\bullet$, ${}^\bullet OH$, H_2O^+ and electrons [5]. All these species posses unpaired electrons, thus being highly reactive *free radicals*. $H^\bullet$ atoms may also be formed by secondary reactions, namely

$$e^-_{aq} + H_3O^+ \quad \longrightarrow \quad H^\bullet + H_2O \tag{4.16}$$

another important secondary reaction is

$$H_2O^+ + H_2O \quad \longrightarrow \quad H_3O^+ + OH^\bullet \tag{4.17}$$

[5] The dot • represents the unpaired electron.

Commonly, there will be a number of reactions among the free radicals themselves, thereby either reconstructing stable water molecules (recombination)

$$e^-_{aq} + H_2O^+ \quad \longrightarrow \quad H_2O \qquad \text{recombination} \tag{4.18}$$

$$H^\bullet + {}^\bullet OH \quad \longrightarrow \quad H_2O \qquad \text{recombination} \tag{4.19}$$

or forming molecular hydrogen:

$$H^\bullet + H^\bullet \quad \longrightarrow \quad H_2 \tag{4.20}$$

$$e^-_{aq} + H_2O^- \quad \longrightarrow \quad H_2 + 2\ {}^-OH \tag{4.21}$$

and hydrogen peroxide:

$${}^\bullet OH + {}^\bullet OH \quad \longrightarrow \quad H_2O_2 \tag{4.22}$$

the last one is an important termination reaction for the ${}^\bullet OH$ radicals. The probability of these reactions depends largely on the local concentrations and are favored within 'spurs', 'blobs' and 'tracks'. Interaction with solutes is only possible if the primary species are able to escape these zones.

The electron is particularly reactive, it captures another water molecule thus forming a negative charged ion

$$H_2O + e^-_{aq} \quad \longrightarrow \quad H_2O^- \tag{4.23}$$

The ions H_2O^+ and H_2O^- are not stable, they do not persist in this form as they dissociate almost immediately (10^{-16} seconds) into H^+ ions and ${}^\bullet OH$ radicals as well as into ${}^-OH$ ions and $H^\bullet$ radicals.

$$H_2O^+ \quad \longrightarrow \quad H^+ + {}^\bullet OH \tag{4.24}$$

$$H_2O^- \quad \longrightarrow \quad H^\bullet + {}^-OH \tag{4.25}$$

The electron in water is normally not free but in a complex with water molecules, i.e. it is *hydrated* which is indicated by the subscript ${}_{aq}$. Since H_2O is a polar

molecule, the electron is able to interact electrostatically with the positive end creating a special spacial structure. This is a dynamical process: the electron is not permanently shielded by the same water molecules, nevertheless, at any moment of time, the electron is surrounded by water dipoles. The hydration shell shields the electron and increases its lifetime which is about $600\,\mu s$.

The reaction of two radical species, such as e^-_{aq}, $H^\bullet$, and $^\bullet OH$, can lead to the production of a stable molecule or an ion. These reactions are diffusion-limited at room temperature. However, the activation energies for all these reactions are well below the activation energy for diffusion, when measured up to $\sim 200^\circ C$. Thus the interactions of free radicals both among themselves and with their own reaction products is dependent primarily on how closely they have been formed. After they are formed, they must diffuse through the medium until they encounter something with which they may interact. The probability of these reactions are favored within spurs, blobs and tracks. Interactions with other solute molecules are only possible, if the primary species are able to escape these zones.

So far only reaction in the absence of oxygen molecules (O^2) have been considered.

Dissolved oxygen is present in our biological samples containing the rods outer segments, because these solutions are prepared at standard air pressure - oxygen is typically dissolved in water at a concentration of $9\,mg/l$ at standard air pressure and at 20^0C. The oxygen molecule is a reaction partner for the primary radiolytic products, the electron and the hydrogen radical:

$$e^-_{aq} + O_2 \quad \longrightarrow \quad O^-_2 \tag{4.26}$$

$$H^\bullet + O_2 \quad \longrightarrow \quad HO^\bullet_2 \tag{4.27}$$

O_2 does not react with the $^\bullet OH$. Equations (4.26) and (4.27) are interrelated

$$HO^\bullet_2 \quad \longrightarrow \quad O^-_2 + H^+ \tag{4.28}$$

In solutions containing oxygen, there is an increased formation of hydrogen peroxide while oxygen is partly regenerated:

$$O^-_2 + O^-_2 + 2\,H^+ \quad \longrightarrow \quad H_2O_2 + O_2 \tag{4.29}$$

$$HO_2^\bullet + HO_2^\bullet \quad \longrightarrow \quad H_2O_2 + O_2 \tag{4.30}$$

The decomposition of H_2O_2 increases the yield of the hydroxyl radical $^\bullet OH$ which may be relevant for the understanding of the role of oxygen in radiation biology.

The rates of the most common chemical reaction in neutral water are displayed in Table 4.1.

Table 4.1: Chemical reaction in water.

Reactions	$\times 10^{10}(M^{-1}s^{-1})$
$e^-_{aq} + e^-_{aq} + 2\,H_2O \longrightarrow H_2 + 2\,OH^-$	0.55
$e^-_{aq} + H^\bullet + H_2O \longrightarrow H_2 + OH^-$	2.5
$e^-_{aq} + H^+ \longrightarrow H^\bullet$	2.3
$e^-_{aq} + OH^\bullet \longrightarrow OH^-$	3
$e^-_{aq} + H_2O_2 \longrightarrow OH^- + OH^\bullet$	1.1
$H^\bullet + H^\bullet \longrightarrow H_2$	0.78
$H^\bullet + OH^\bullet \longrightarrow H_2O$	2
$H^+ + OH^- \longrightarrow H_2O$	14.3
$OH^\bullet + OH^\bullet \longrightarrow H_2O_2$	0.55

4.6 Direct and indirect effect

As shown in the preceding section, highly reactive species are formed by water radiolysis. They are not only able to react with each other but also with solute molecules. Thus biological key substances cannot only be inactivated by direct energy absorption but also via interaction with radicals formed in their environment. Because of their high water content, as already mentioned in other occasions above, this should be especially so in cells. Therefore is possible, in principle, to distinguish between *direct* and *indirect* radiation inactivations [35].

We consider N, the number of intact entities in a solution of volume V, N^+ the number of inactivated molecules, $\overline{N}^+$ the respective mean value. The 'surviving

fraction' y is then:

$$y = \frac{N - N^+}{N} \simeq e^{-\overline{N}^+/N} \tag{4.31}$$

For the *direct* effect the assumption is that the number of inactivated molecules is proportional to the dose:

$$\overline{N}^+ = 1 - \alpha \cdot D \cdot N \tag{4.32}$$

thus, for the *direct* effect one finds:

$$y = -\alpha \cdot D \tag{4.33}$$

this means that the surviving factor y is only a function of dose and independent of concentration. The fraction of damaged molecules, on the other hand, is:

$$\frac{\overline{N}^+}{N} = 1 - e^{-\alpha D} \tag{4.34}$$

the same holds, of course, for the percentage of damaged entities, which differs from the fraction for a factor 100.

Now let's consider the (*indirect*) effect of the radicals. If the concentration of the radicals is not too high, each radical will react with the solute molecules with a certain probability to inactivate them. This means that not the fraction, but the mean number of destroyed entities is linearly related to the dose; thus for the surviving factor we have

$$y = e^{-\beta D/N} \tag{4.35}$$

or, considering the fraction of damaged entities:

$$\frac{\overline{N}^+}{N} = 1 - e^{-\frac{\beta D V}{N c}} \tag{4.36}$$

So we expect that the effect of the radicals produced in a biological tissue increases by increasing the concentration of the sensitive entities. Normally, in the cellular systems the intracellular concentration cannot be easily varied. Otherwise the samples of ROS in solutions are available in different concentrations of rhodopsin.

Now we have to anticipate how rhodopsin could be sensitive to the radicals produced in the irradiation experiments. Our thesis, as diffusively explained in chapter 5, is that the radicals in the ROS solutions react with the lipids in the rods

causing lipid peroxidation which results in chemiluminescence, that is the production of photons in the visible range which are able to bleach the retinal present in the molcules of rhodopsin into the rods. So the final effect of the radicals yield is the bleaching of the rhodopsin molecules.This final effect is detectable spectroscopically, as explained in 2.1.

4.7 Yield of hydroxyl radicals

For our purposes we will use the estimations of the yield of OH radical induced by ionizing radiation calculated in [46]. This paper deals with an empirical model, and calculations consist in a combination from the yield from the incident primary particle plus a contribution from a secondary yield from a secondary electron. The calculations have been developed for heavy ions, including carbon ion. At energies higher than $1\,MeV/n$ the simulated values are in reasonably good agreement - within 10% - with the experimental yields of heavy ions considered. The geometrical size of the spur and the initial yields of species at $10^{-12}s$ were assumed to be the same for all incoming projectiles, but depending on the species of the products. These values for OH radical is shown in Table 4.2.

Table 4.2: Diffusion constant, initial radii in a spur at $1\,ns$.

Species	$D \cdot 10^5 (cm^2 s^{-1})$	$r_0(nm)$
e^-_{aq}	4.5	6.0
$OH^\bullet$	2.8	4.0

Figure 4.5 shows the predicted yields of species due to radiolysis of water as a function of initial energy at nanoseconds produced by proton (solid lines) and carbon (dotted lines). Proton and carbon ion of the same specific energy (keV/n) travels at the same velocity. It was seen that dependences of the yields of species on specific energy were different between proton and carbon ion even though they traveled at the same velocity.

Figure 4.6 shows the $G(OH)$ for heavy ions at microseconds: the agreement with

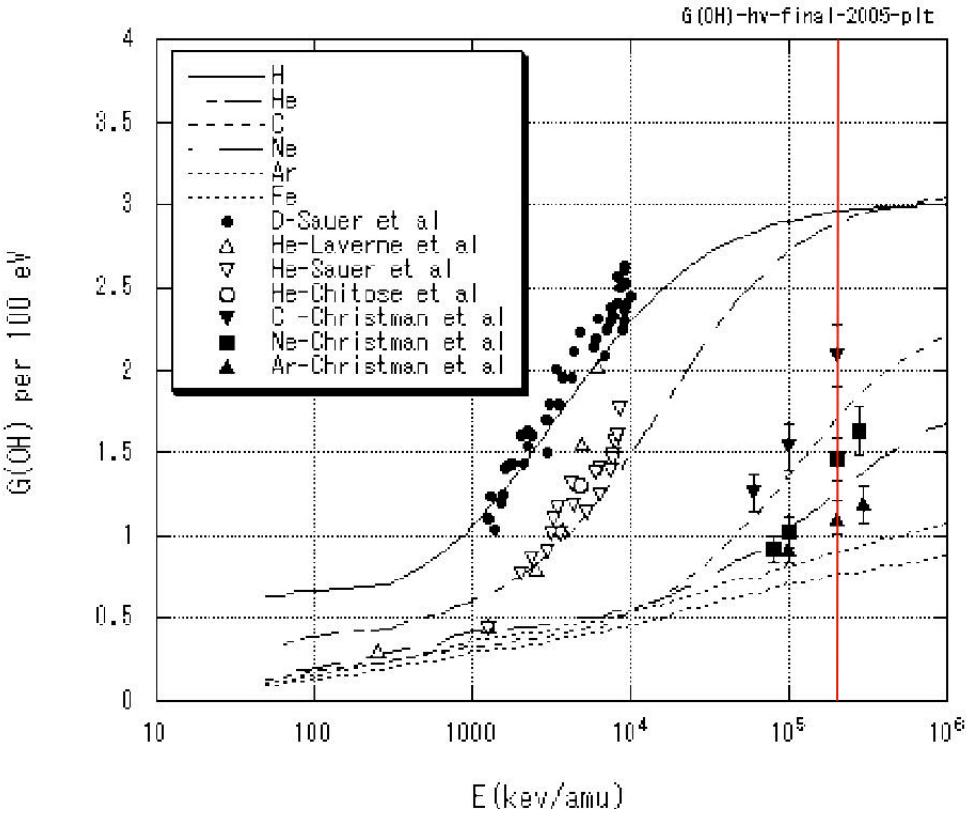

Figure 4.5: Calculated yields , $G(OH)$ at microseconds, for protons, helium-, carbon-, neon-, argon-, and iron-ions, and experimental data. The vertical red line crosses the curves at the values corresponding to $E = 200\,MeV/n$. From [46].

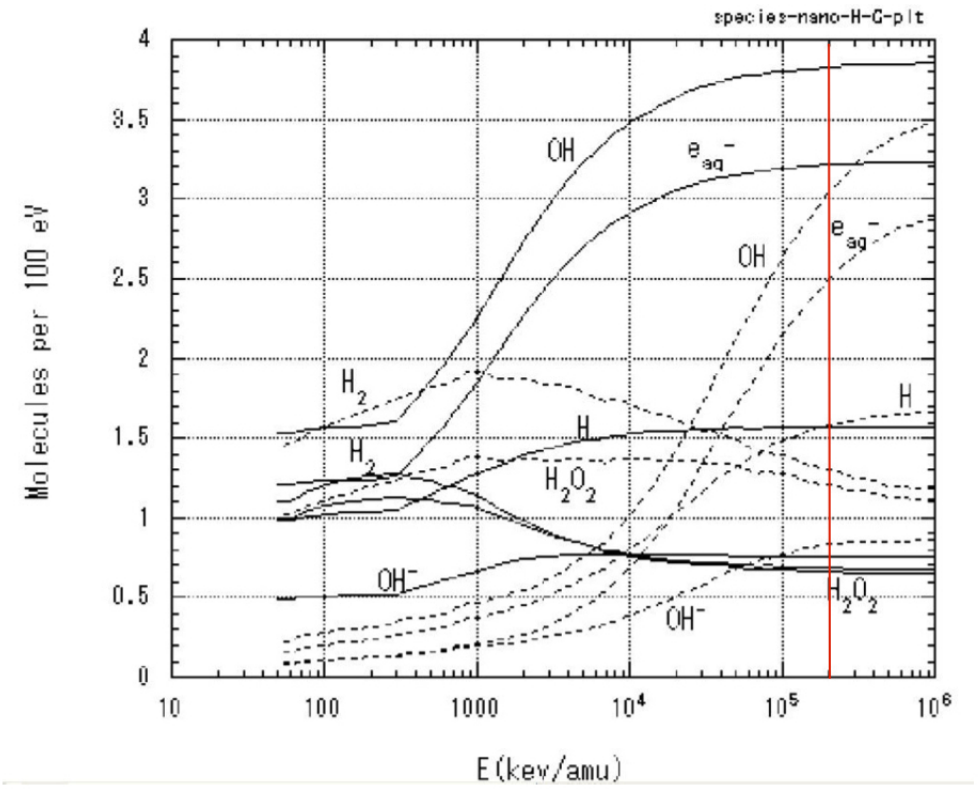

Figure 4.6: Calculated yields of species at nanoseconds, produced by radiolysis of water with protons (solid line) and carbon (dotted line), as a function of specific energy. The vertical red line crosses the curves at the values corresponding to $E = 200\,MeV/n$. From [46].

experiments is also visible. The yields of OH radical have been estimated at two representative times, nanoseconds and microseconds after irradiation: the former may be relevant in case the period of formation of DNA initial damage and the latter to the period in which chemical reactions are in equilibrium in a uniform bulk solution. From the comparison of the G-value depicted in 4.5 e 4.6 a time-dependent decay is clearly seen, as expected. Assuming the data from [46], we can estimate from the figures the yields of OH radicals to apply to our case (the red lines in the figures 4.5 and 4.6 cross the curves of the OH yields at the energy of interest). We deal with $200\,MeV/n$ carbon ion, so, considering the calculated data affected by an error of $\approx 10\%$ [46], we can suppose

$$G(OH)_{@ns} = (3.0 \pm 0.3)\,\frac{molecules}{100\,eV} \tag{4.37}$$

$$G(OH)_{@\mu s} = (1.8 \pm 0.2)\,\frac{molecules}{100\,eV} \tag{4.38}$$

Now we can apply these results to our system. As shown in section 4.2, the LET released in each vials subjected to irradiation of carbon ions at $200\,MeV/n$ is $\approx 17\,keV/\mu m$. If we consider that the path is $3\,cm$ long, we obtain the released energy in the sample: $E \approx 17\,keV/\mu m \cdot 3\,10^4 \mu m \approx 5\,10^8\,eV$.

Using the estimation of the formula 4.38 we obtain the approximate number of altered entities (in our case hydroxyl radical $OH^\bullet$) produced in the suspension: $(OH^\bullet)\,entities \approx 2 \cdot 5 \cdot 10^8\,eV/(100\,eV) \approx 10^7$; that is to say that each carbon particle in its path through the sample produces ten million of hydroxyl radical.

As will be described in the following chapter - see the section 5.3 -, we performed carbon ion irradiation of samples of ROS in suspension at different fluences of particles: $flu1 \approx 1.5 \cdot 10^8$ ions/spill; $flu2 \approx 9 \cdot 10^6$ ions/spill; $flu3 \approx 4.7 \cdot 10^5$ ions/spill; the spill length was $\approx 1\,s$. Thus, multiplying the fluences by the yield of a single carbon ion and dividing by 10^6, we obtain the amount of free radicals $OH^\bullet$ totally produced in the interval of time of $1\,\mu s$. From these data, knowing the volume of the sample, that is $V_{sample} = 1\,ml$, we can find the relative molar concentration of $OH^\bullet$. Because of the stability of the process of bleaching of the rhodopsin molecule inside the ROS we can integrate the values of this concentration in the whole interval of

$1\,s$, obtaining:

$$c_{OH^\bullet}(flu1) \approx \frac{10^7 \cdot flu1}{\mathcal{N}_A \cdot V_{sample}} \approx 2.5\,\mu M/l \tag{4.39}$$

$$c_{OH^\bullet}(flu2) \approx \frac{10^7 \cdot flu2}{\mathcal{N}_A \cdot V_{sample}} \approx 0.2\,\mu M/l \tag{4.40}$$

$$c_{OH^\bullet}(flu3) \approx \frac{10^7 \cdot flu3}{\mathcal{N}_A \cdot V_{sample}} \approx 8\,nM/l \tag{4.41}$$

where $\mathcal{N}_A$ is the Avogadro number.

We can also estimate the displacement in the space of the initial spurs of the radicals $OH^\bullet$ produced. From the table 4.2 the value of the spur radius of each hydroxyl radical is (at $1\,ns$) $r_0 = 4\,nm = 4 \cdot 10^{-9} m$. On the other side the total irradiated area is about $0.5\,cm$ of diameter, so we can indicate the radius of the total irradiated area $r_T \approx 0.3\,cm = 3 \cdot 10^{-3} m$. We can also consider the maximum extension of the area of interaction around the track of every incident ions, that is the penumbra radius x_p expressed in the formula 4.4. In the case of carbon ions at a specific energy of $200\,MeV/n$, we have $x_p \approx 0.5\,mm = 5 \cdot 10^{-4} m$.

From these considerations we can think about the section of the irradiated volumes, perpendicularly to the direction of the impinging particles; so we evaluate the ratio of the penumbra area A_p to the area of the spur of a hydroxyl radical A_0: $A_p/A_0 \approx 10^{10}$: this means that in each penumbra a generic spur of $OH^\bullet$ radical is very rare and isolated, very 'far' from other spurs. To see this if we consider the LET in a path of $1\,mm$ and insert this value in the formula 4.37 we obtain a yield of about $10^4 \div 10^5$, five orders of magnitude smaller than 10^{10} found before. We can add that the ratio of the total area A_T to the penumbra area A_p is about 40. Also the rate of the chemical reactions of recombination, for the amount of molar concentration found and time interval of the order of the nano-seconds, are very small, as shown in table 4.1. All these considerations are to conclude that, even at the higher fluences (that is $\approx 10^8$ ions/spill), all the radicals produced by the ions are available to react with the medium because of the superpositions of their spurs and hence the radical recombinations are very improbable.

This result will be used later in the section 5.3 where the experimental data are discussed.

Chapter 5

Radiation experiments on rod outer segment

5.1 ROS samples and experimental sessions

Section 2.1 provides the description of the preparation of ROS samples from bovine retinae and the spectroscopic evaluation of the amount of the chromophores. The preparation and storage of the samples took place in the laboratories of the Biology Department of the University of Tor Vergata. The ROS samples, coming from the batch solution, prepared at different dilution, were stored in black painted boron silicate glass vials (purchased from SUN SRI, TN, USA) to avoid light exposure, each containing $1\,ml$ of suspension. The ROS samples were then delivered in an accelerator and then irradiated. After that they were and spectroscopically analyzed in a laboratory of the Tor Vergata University, as explained below in some detail. All the samples were stored in dry ice during the transport, thawed just before use and then refreezed till spectrophotometrical measures were performed.

Two main experimental sessions have been carried out: on february 2006 and on february 2007. Both of them took place at Darmstadt, in Germany, at the Gesellschaft fur Schwerionenforschung mbH (GSI)/Biophysik. The first run session was devoted to perform the preliminary tests of the efficiency of the procedure. In both the sessions carbon-ions at $200\,MeV/n$ have been used.

During the irradiation the vials were positioned in front of the ion beam exit,

with their axes along the beam direction. In the calculations we apply the LET value acquired in section 4.1 from SRIM simulations, $LET = (17.4 \pm 1.6)\, keV/\mu m$). We utilize the formula 4.2 for the delivered dose computations, with the application of the error propagation, to take into account the uncertainty in the LET value and in the number of delivered ions, known with an accuracy dependent on the error of the charge delivered by the accelerator and measured by the beam devices, during the beam emission: an error of $\Delta ions = 10^5$ has been calculated[1].

5.2 Run session of February 2006

The following table 5.1 presents the irradiation scheme of the run session of February 2006. As said above it was a preliminary test. All the 28 samples (prepared at two different rhodopsin concentration, $c_1 \approx 0.8\mu M$ and $c_2 \approx 0.6\mu M$) underwent the same protocol during the transport and the irradiation, except for *control* samples which have not been irradiated. Samples 18 and 28 were damaged. In the same table also the calculated dose delivered in each sample is showed.

The spectroscopy measurements after radiation exposure were performed as illustrated in section 2.1: in dark conditions; after exposure to light; after the addition of the excess of 11-cis-retinal (regeneration); and after a second exposure to light. The qualitative evaluation of the success of the regeneration process is also listed in table 5.1.

In figure 5.1 there is the irradiation profile: the two groups at different concentrations are distinguishable. The beam of particles has been directed in front of the vials, along their axis; the vials were positioned horizontally in a dedicated grid, and the pointing procedures of the beam were performed in remote control, from the 'control room'. The number of ions, used to obtain the absorbed dose expressed in gray in the table, has been calculated from the amount of charge delivered at every spill of particles of ^{12}C(these data have been furnished by a dedicated detector in the beam line). In the calculations we took into account a geometrical factor 0.5,

[1]This calculation is derived from the fact that charge per spill, expressed in nC, has the accuracy of about 10%.

Table 5.1: Run session of February 2006, ^{12}C-ion irradiation scheme.

$c_1 \approx 0.8\,\mu M$				$c_2 \approx 0.6\,\mu M$			
Samples	Spills	Dose (Gy)	Reg.	Samples	Spills	Dose (Gy)	Reg.
1 ctr	0	-	yes	15 ctr	0	-	yes
2	1	8 ± 2	yes	16	1	4 ± 1	yes
3	2	17 ± 3	yes	17	2	7 ± 1	no
4	4	33 ± 6	yes	18*	4	-	-
5	8	$(7 \pm 1)10$	yes	19	8	31 ± 6	yes
6	16	$(13 \pm 3)10$	no	20	16	$(6 \pm 1)10$	yes
7	32	$(26 \pm 5)10$	no	21	32	$(12 \pm 2)10$	yes
8 ctr	0	-	yes	22 ctr	0	-	yes
9	2048	$(11 \pm 2)10^3$	no	23	2048	$(7 \pm 1)10^3$	no
10	1024	$(40 \pm 8)10^2$	no	24	1024	$(35 \pm 7)10^2$	no
11	512	$(20 \pm 3)10^2$	no	25	512	$(17 \pm 3)10^2$	no
12	256	$(10 \pm 2)10^2$	no	26	256	$(9 \pm 1)10^2$	no
13	128	$(5 \pm 1)10^2$	no	27	128	$(40 \pm 8)10$	no
14	97	$(40 \pm 7)10$	no	28*	67	-	-
ctr is for control; *Reg.* is for regeneration; * indicates damaged vials							

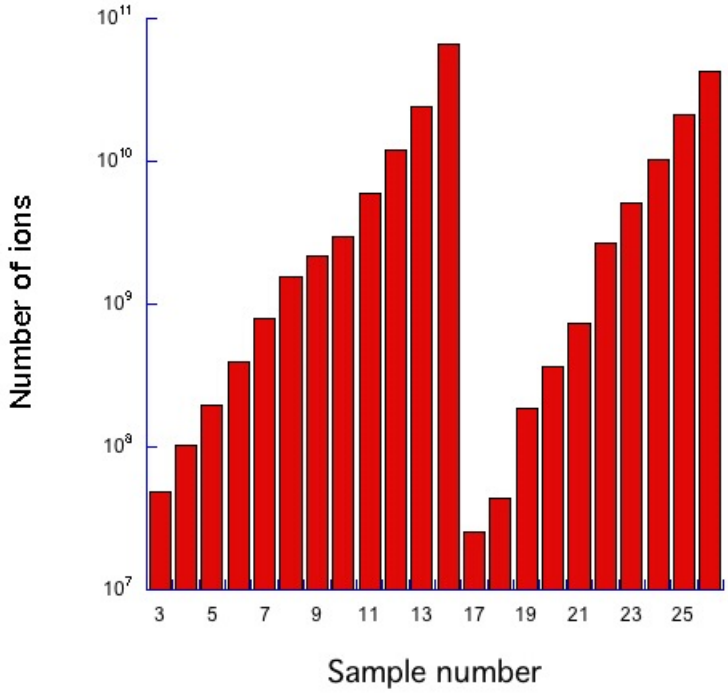

Figure 5.1: Plot of the number of ions received by each vial. Two groups are distinguishable: samples 1-14 and 15-18, see table 5.1.

for the reason that the vials were about 1/2 full.

The absorbed dose has a range of approximately four decades: the minimum dose delivered is $(4 \pm 1)\,Gy$, corresponding to one spill of ^{12}C ions; the maximum dose delivered is $(11 \pm 2) \cdot 10^3\,Gy$, corresponding to the emission of 2048 spills on sample 9.

Except for sample 17 - which probably was damaged under the manipulation and/or the storage -, it seems that regeneration happens until the dose passes a threshold value: roughly, the lowest absorbed dose leading to no regeneration was $(66 \pm 6)\,Gy$ for the samples 6 with concentration c_1; and $(12 \pm 2)\,10\,Gy$ for the sample 27 with concentration c_2.

5.3 Session of February 2007

Table 5.2 and table 5.3 present the scheme of the irradiation session carried out at the GSI on February 2007. In this case four series of samples, at different concentrations, were extracted from the batch solution: two from the top (Super-1 e Super-2) and two from the bottom (Fondo-1 e Fondo-2) of the batch. In total 90 vials of ROS samples were prepared, but only 60 of them have been utilized for the whole procedures; the relative tags and information on irradiation are available in the tables. All the samples underwent ^{12}C-ion at $200\,MeV/n$ irradiation.

We also report on the beam properties: the interval between two consecutive spills was $ISI \approx 2.7\,s$; the spill length was $\approx 1.1\,s$ and the spill diameter $\approx 1\,cm$. Moreover, we set a geometrical factor of 0.5, to take into account the fact that approximately only half of the vials were full. In figure 5.2 the number of ions per vial is presented. The number of ions varies from $2.4 \cdot 10^5$ to $4.1 \cdot 10^8$.

As above, for each sample we evaluated the absorbed dose using the delivered charge, that is the number of ions. The figure 5.2 shows the irradiation profile regarding the dose absorbed by the samples. The dose values range approximately from $\approx 0.02\,Gy$ for the first sample to $\approx 3\,Gy$, for the last one, extending over about three decades. The amount of the maximum dose absorbed with respect the previous data form february 2006 session is much smaller, at least 3 order of magnitude and

Table 5.2: Session of February 2007, Samples Super-1 and Super-2. All samples have been regenerated.

SUPER 1				SUPER 2			
Samples	Spills	Fluence*	Dose (Gy)	Samples	Spills	Fluence	Dose (Gy)
ctr	0	0	-	ctr	0	0	-
1	1	flu1	$(69 \pm 6)10^{-1}$	2	1	flu1	$(68 \pm 6)10^{-1}$
7	2	flu1	14 ± 1	8	2	flu1	14 ± 1
13	3	flu1	20 ± 2	14	3	flu1	20 ± 2
19	4	flu1	26 ± 2	20	4	flu1	27 ± 2
25	5	flu1	33 ± 3	26	5	flu1	34 ± 3
31	1	flu2	$(40 \pm 4)10^{-2}$	32	1	flu2	$(40 \pm 4)10^{-2}$
37	2	flu2	$(76 \pm 7)10^{-2}$	38	2	flu2	$(80 \pm 8)10^{-2}$
43	3	flu2	$(11 \pm 1)10^{-1}$	44	3	flu2	$(11 \pm 1)10^{-1}$
49	4	flu2	$(15 \pm 1)10^{-1}$	50	4	flu2	$(15 \pm 1)10^{-1}$
55	5	flu2	$(19 \pm 2)10^{-1}$	56	5	flu2	$(18 \pm 2)10^{-1}$
61	1	flu3	$(22 \pm 2)10^{-3}$	62	1	flu3	$(22 \pm 2)10^{-3}$
67	2	flu3	$(42 \pm 4)10^{-3}$	68	2	flu3	$(40 \pm 4)10^{-3}$
73	3	flu3	$(58 \pm 5)10^{-3}$	74	3	flu3	$(60 \pm 6)10^{-3}$
79	4	flu3	$(81 \pm 7)10^{-3}$	80	4	flu3	$(81 \pm 7)10^{-3}$
85	5	flu3	$(99 \pm 9)10^{-3}$	86	5	flu3	$(98 \pm 9)10^{-3}$
ctr is for control; *$flu1 \approx 1.5 \cdot 10^8$ ions/spill; $flu2 \approx 9 \cdot 10^6$ ions/spill; $flu3 \approx 4.7 \cdot 10^5$ ions/spill							

are below the threshold values discussed above for the regeneration. So the fact that all the samples listed in table 5.3 underwent regeneration is not surprising.

To compare the absorbance peak, as already made for the samples of the preceding session, we superimpose the absorbance curves in the isosbestic point.

From the ΔA_{500nm} for the control samples, the original concentrations of active molecules have been evaluated:

Table 5.3: Session of February 2007, Samples Fondo-1 and Fondo-2. All samples have been regenerated.

FONDO 1				FONDO 2			
Samples	Spills	Fluence*	Dose (Gy)	Samples	Spills	Fluence	Dose (Gy)
ctr	0	0	-	ctr	0	0	-
3	1	flu1	$(68 \pm 6)10^{-1}$	4	1	flu1	$(69 \pm 6)10^{-1}$
9	2	flu1	14 ± 1	10	2	flu1	14 ± 1
15	3	flu1	20 ± 2	16	3	flu1	20 ± 2
21	4	flu1	28 ± 3	22	4	flu1	27 ± 3
27	5	flu1	34 ± 3	28	5	flu1	33 ± 3
33	1	flu2	$(41 \pm 4)10^{-2}$	34	1	flu2	$(40 \pm 4)10^{-2}$
39	2	flu2	$(73 \pm 7)10^{-2}$	40	2	flu2	$(74 \pm 7)10^{-2}$
45	3	flu2	$(11 \pm 1)10^{-1}$	46	3	flu2	$(11 \pm 1)10^{-1}$
51	4	flu2	$(15 \pm 1)10^{-1}$	52	4	flu2	$(15 \pm 1)10^{-1}$
57	5	flu2	$(20 \pm 2)10^{-1}$	58	5	flu2	$(20 \pm 2)10^{-1}$
63	1	flu3	$(20 \pm 2)10^{-3}$	64	1	flu3	$(20 \pm 2)10^{-3}$
69	2	flu3	$(40 \pm 4)10^{-3}$	70	2	flu3	$(40 \pm 4)10^{-3}$
75	3	flu3	$(57 \pm 5)10^{-3}$	76	3	flu3	$(58 \pm 5)10^{-3}$
81	4	flu3	$(79 \pm 7)10^{-3}$	82	4	flu3	$(77 \pm 7)10^{-3}$
87	5	flu3	$(95 \pm 9)10^{-3}$	88	5	flu3	$(33 \pm 3)10^{-3}$
ctr is for control; *$flu1 \approx 1.5 \cdot 10^8$ ions/spill; $flu2 \approx 9 \cdot 10^6$ ions/spill; $flu3 \approx 4.7 \cdot 10^5$ ions/spill							

- $c_{Super-1} = (1.80 \pm 0.02)\mu M$
- $c_{Super-2} = (1.92 \pm 0.02)\mu M$

We notice that for the data belonging to the groups Fondo-1 and Fondo-2, the spectroscopic measurements are very noisy or not convincing: the curves are not smooth, probably because of the major opacity of the suspensions, obtained, as

mentioned above, from the bottom of the batch. For these samples we estimated two less accurate values: $c_{Fondo-1} \approx (5.3 \pm 0.5)\mu M$ and $c_{Fondo-2} \approx (3.1 \pm 0.5)\mu M$.

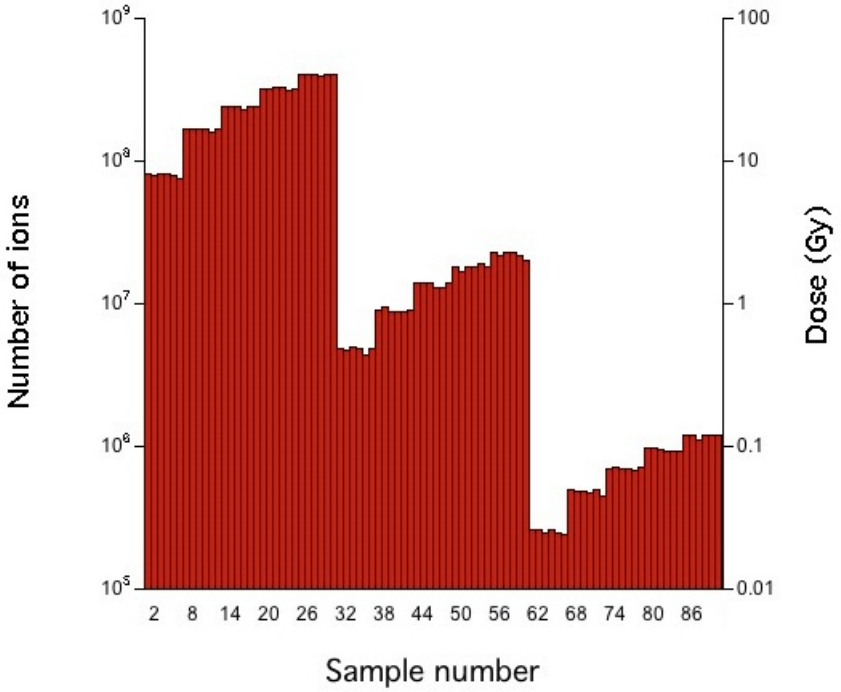

Figure 5.2: Plot of the number of ions received (left axis) by each vial, ordered by samples number, that is in time. The fluences in the three groups of vials (1-30; 31-60; 61-90) are respectively: $1.5 \cdot 10^8$ ions/spill; $9 \cdot 10^6$ ions/spill; $4.7 \cdot 10^5$ ions/spill as it can be seen in the above tables. The delivered dose (right axis) varies from $\approx 0.02\,Gy$, to $\approx 34\,Gy$, covering three decades

5.4 Discussions and results

The absorbing spectrum of the irradiated samples in the range $(400 \div 650)\,nm$ has been evaluated for each samples coming from the irradiation sessions in the accelerators. After the first spectroscopic measurements, all the samples were exposed to light for a time adequate to obtain the bleaching of the samples. After that new spectroscopic measurements of the spectrum were performed. In this way a comparison of the spectra before and after the total bleaching is possible. In particular the

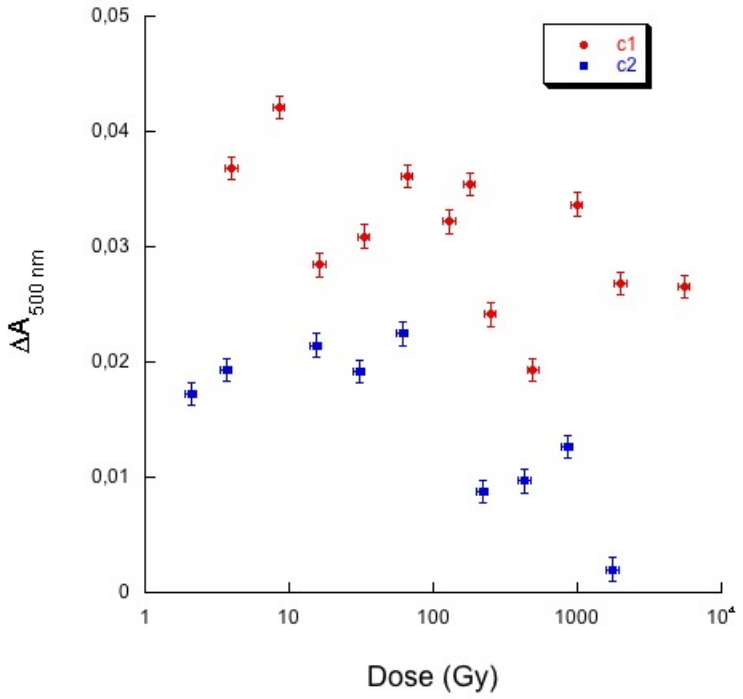

Figure 5.3: February 2006. Radiation-induced isomerization of retinal in two series of samples at different concentrations. The amount of the isomerization events is given by the difference of the absorbance at 500 nm of the irradiated samples before and after exposure to light versus the absorbed dose. $c_1 \approx 0.8\,\mu M$ and $c_2 \approx 0.6\,\mu M$.

absorbance at 500 nm, A_{500nm} has been evaluated: the difference ΔA_{500nm} between the values A_{500nm} before and after exposure to light gives the quantitative measure of the active rhodopsin molecules are in the sample after the irradiation process. In order obtain these differences, the absorbance spectra have been vertically shifted to superimpose them in the isosbestic point, as discussed in section 2.1 (see figures 2.5, and 2.8). This procedure has been repeated for both the data of the session of february 2006 and the data of session of february 2007.

In the figure 5.3 the the difference between the absorbance at 500 nm, ΔA_{500nm}, before and after exposure to light is plotted versus the amount of absorbed dose for each of the samples of the run of february 2006. Sample 23 shows an anomalous spectrum, so it has been excluded from the plot. The behavior of the dose-response at high doses for the samples at concentration c_1 seems to be anomalous. As men-

tioned before, these data belong to a preliminary run session aimed at improving the the efficiency of the whole procedure.

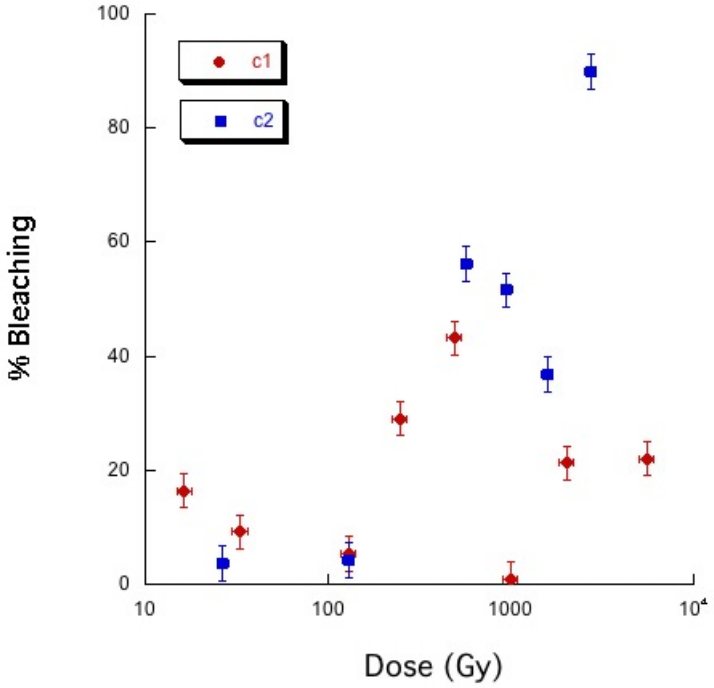

Figure 5.4: February 2006. Radiation-induced isomerization of retinal in two series of samples at different concentrations. The percentage of bleaching is displayed. $c_1 \approx 0.8\,\mu M$ and $c_2 \approx 0.6\,\mu M$.

From the figure 5.3 we can observe that the samples with different concentrations seem to have different features as far as concerned the radiation inactivation, evaluated by ΔA_{500nm}.

To correctly investigate the correlation between the efficiency of radiation with respect the bleaching and the concentration of rhodopsin in the irradiated samples, we consider the percentage of bleaching. In figure 5.4 the percentage of bleaching is displayed in function of the absorbed dose. From this figure we hardly could find a common behavior of the samples belonging to the same group. On the other hand, we have to consider that c_1 and c_2 differ one onother for $\approx$ 25% and that for the consideration discussed in the section 4.33 due to an indirect effect of radiation the number of inactivated entities will depend on the concentration.

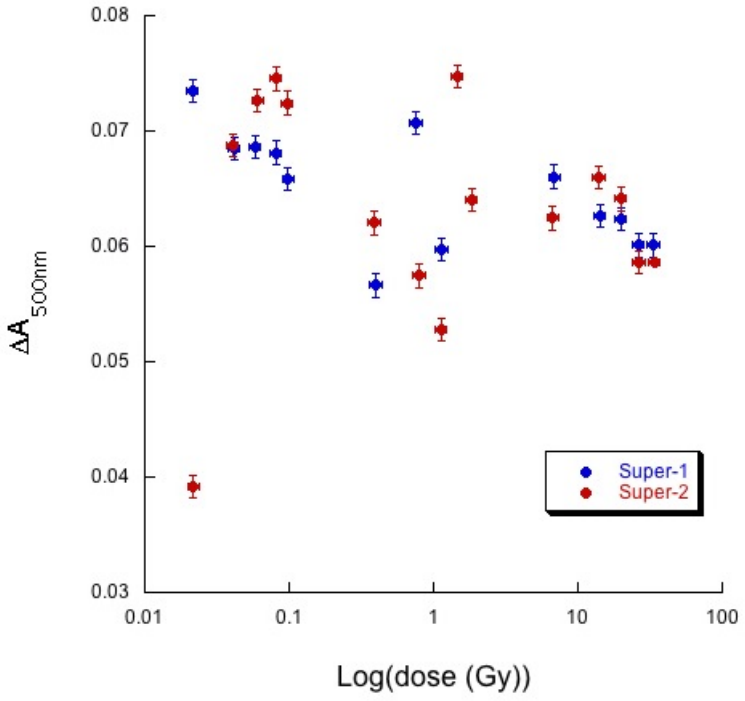

Figure 5.5: February 2007. For each irradiated sample the difference of the absorbance at $500\,nm$ before and after exposure to light versus the absorbed dose (in logarithmic scale). Only selected samples are considered, as discussed in the text. $c_{Super-1} \approx 1.8\,\mu M$, $c_{Super-2} \approx 1.9\,\mu M$.

If we try the same analysis for the data from the session of february 2007 we obtain the figure 5.5. Here we focus on Super-1 e Super-2 data, excluding sample 49, sample 55 and sample 62, for the reasons mentioned above. We observe that the group Super-1 is characterized by a higher concentration than Super-2, and that $c_{Super-1}$ and $c_{Super-2}$ differ only for $\approx 6\%$.

We can notice again, as already for the preceding session data, that the plot of the percentage of bleaching versus dose is more interesting and useful. So we elaborate the data shown in figure 5.6. We have already mentioned that the data of the two groups Fondo-1 and Fondo-2 do not show smooth spectra, so we apply an error of 3%, while for the data of Super-1 and Super-2 we have 1%. In addiction we note that the percentage is not applicable for the data of Fondo-2 because of the not convincing spectra of the control samples, which do not provide a true value of

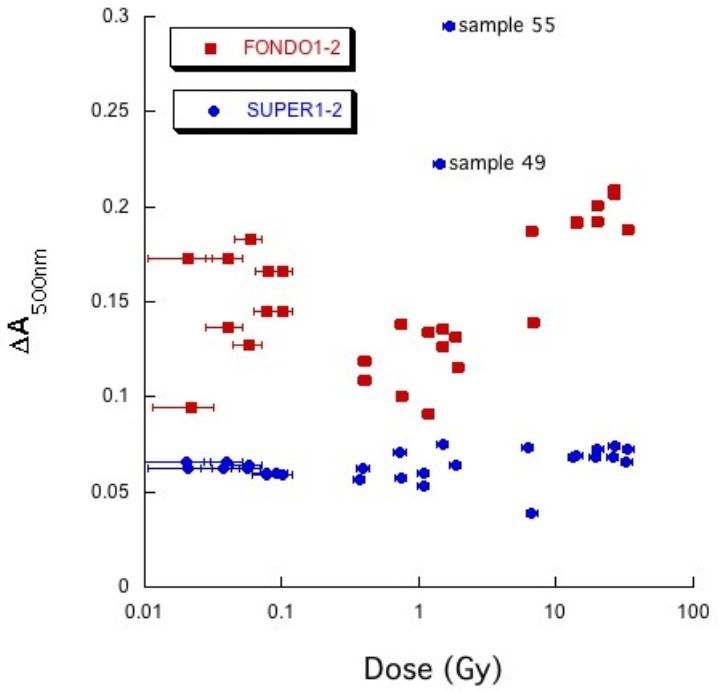

Figure 5.6: February 2007. Radiation-induced isomerization of retinal in two series of samples at different concentrations. $c_{Super-1} \approx 1.8\,\mu M$, $c_{Super-2} \approx 1.9\,\mu M$; $c_{Fondo-1} \approx 5.3\,\mu M$ and $c_{Fondo-2} \approx 3.1\,\mu M$. Also the 'anomalous' samples 49 and 55 are indicated.

the concentration. So in the figure 5.7 we show Super-1, Super-2 and Fondo-1 data.

From the analysis of the figure 5.7 is difficult to see an increasing of the percentage of bleaching proportional to the absorbed dose, on this topic we will discuss in the following. In any case we can observe a suggestion that the samples characterized by a major concentration in rhodopsin are affected more significantly by ionizing radiation. This evidence is in accordance with an indirect effect of the radiation on the rhodopsin molecules, as discussed above in the section 4.6. This seems to confirm the idea that the bleaching is ascribable to the action of the free radicals, the principal indirect cause of the passage of the ionizing particles in the biological tissue, as we explain in detail in the next chapter. This behavior of a major bleaching for the more concentrated suspensions holds almost in the whole range of dose, at

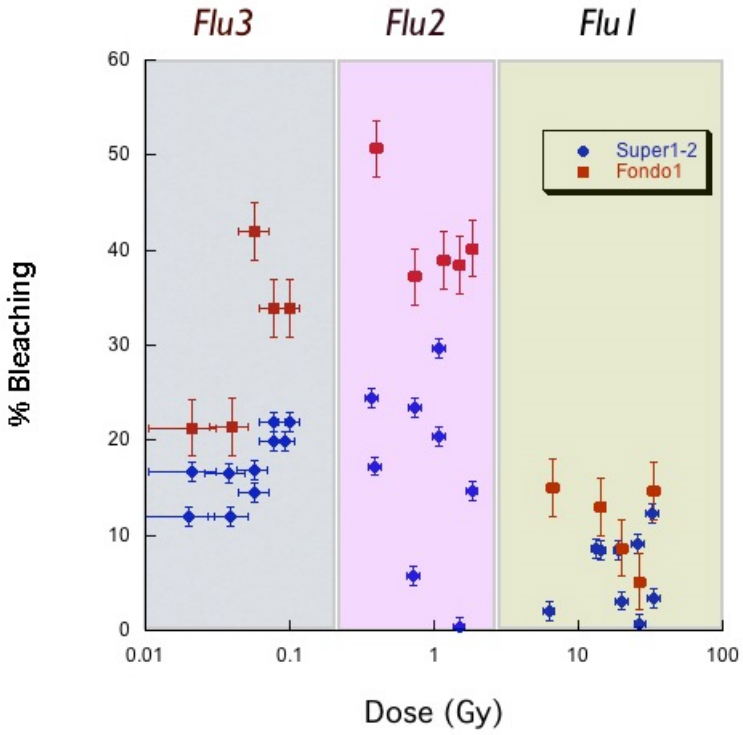

Figure 5.7: February 2007. Radiation-induced isomerization of retinal in two series of samples at different concentrations. The percentage of bleaching is displayed. $c_{Super-1} \approx 1.8\,\mu M$, $c_{Super-2} \approx 1.9\,\mu M$ and $c_{Fondo-1} \approx 5.3\,\mu M$.

the different fluences used.

In figure 5.7 the colored areas indicate the different fluences used during the irradiation. It appears anomalous the fact that the dose delivered at the higher fluence (fluence 1) seems to be less efficient than the energy delivered at lower fluences.

In the attempt to find the relation between the inactivation (bleaching) of the rhodopsin molecules and the delivered energy, we consider the different fluences separately.

Starting from the lowest fluence (flu3$\approx 4.7{\cdot}10^5$ ions/spill) in figure 5.8 we observe the behavior of samples Super-1 and Super-2 in a linear scale.

In figure 5.9 relative to fluence2$\approx 9\,10^6 ions/spill$ neither Super-1 data nor Super-2 data show a linear trend with respect dose.

In figure 5.10 both Super-1 and Super-2 (with the exception of the first value at

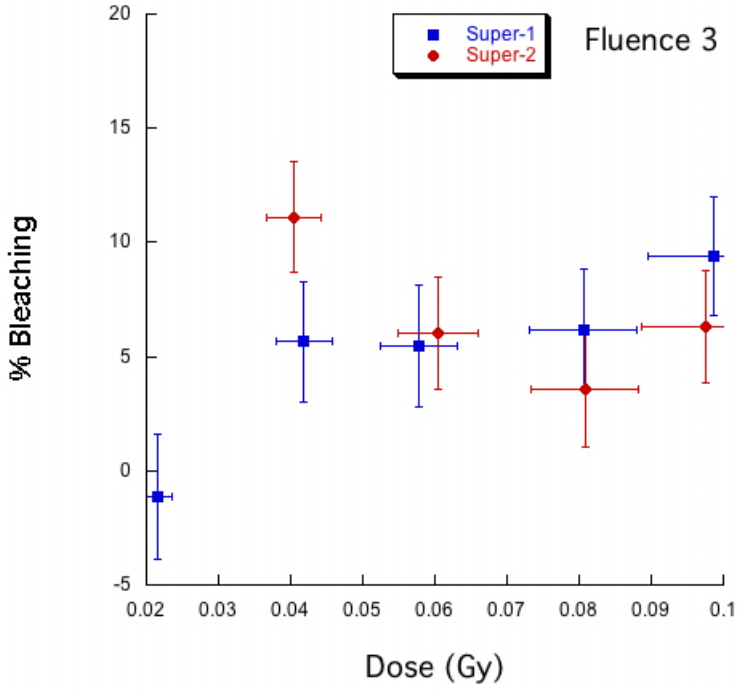

Figure 5.8: Rhodopsin bleaching vs dose, using fluence1$\approx 4.7 \cdot 10^5$ ions/spill

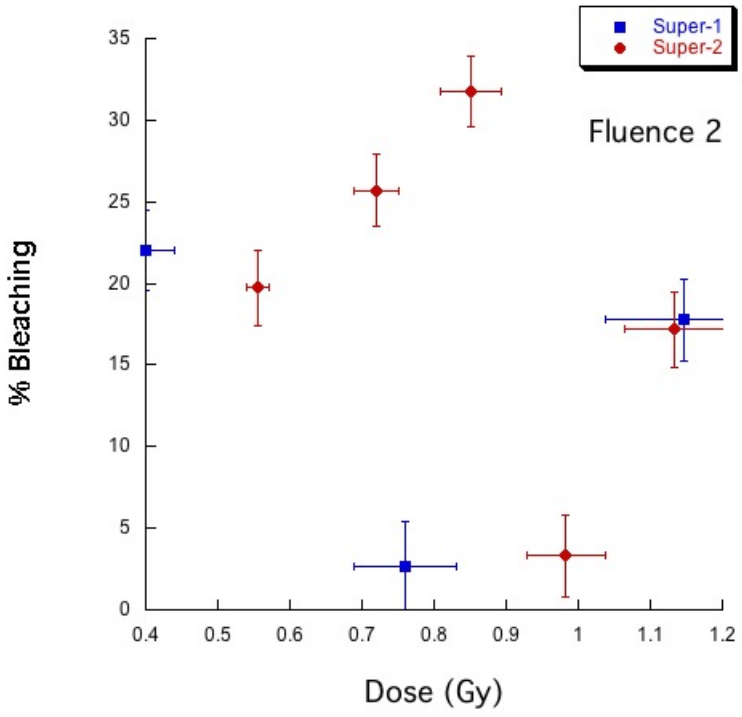

Figure 5.9: Rhodopsin bleaching vs dose, using fluence2$\approx 9 \cdot 10^6$ ions/spill

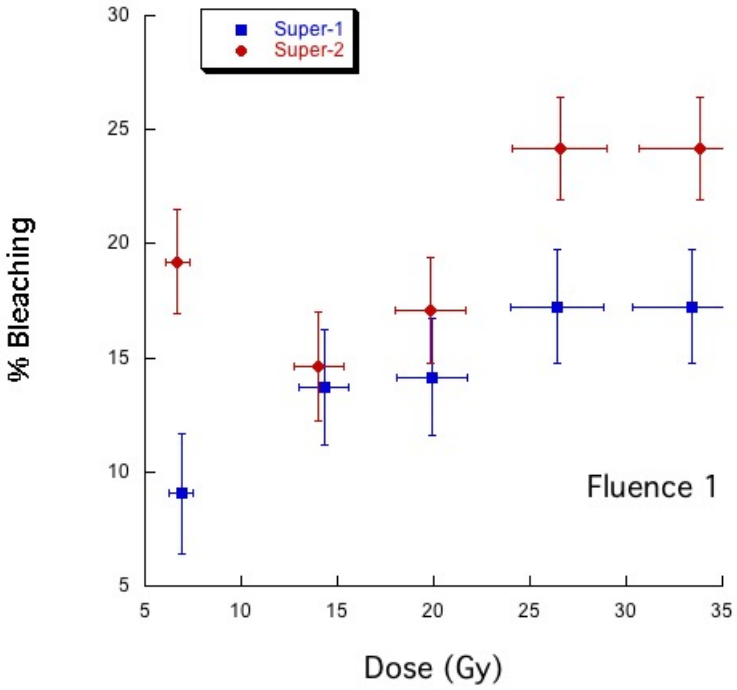

Figure 5.10: Rhodopsin bleaching vs dose, using fluence1$\approx 1.5 \cdot 10^8$ ions/spill

$\approx 6.7\,Gy$) exhibit a linear proportionality to the dose.

The examinations of figures 5.10, 5.9 and 5.8 lead us to consider only the samples belonging to the group Super-1, and to include the data obtained at fluence 3 and fluence 1 to best investigate the relations between delivered dose and amount of bleached entities. The plot of the percentage of bleaching of the samples Super-1 at the lower and the higher fluences is displayed in figure 5.11. As already mentioned, the delivered doses extend over a range of almost four decades (from $\approx 2 \cdot 10^{-2}\,Gy$ to $\approx 3 \cdot 10^{1}\,Gy$). So, for clarity, the selected data in figure 5.11 are shown in a semi-logarithmic scale.

The relation between percent of rhodopsin bleached by carbon ions irradiation and dose, is different for different fluences. In figure 5.12 this effect is emphasized by two raw regression lines, which impose a linear proportionality and force line fit through zero. From the analysis of the two figures 5.11 and 5.12 we can say that the irradiation at low fluence results more efficient than that at high fluence. Fluence1 is nearly 300 times greater than Fluence3; while the linear coefficients differ of a

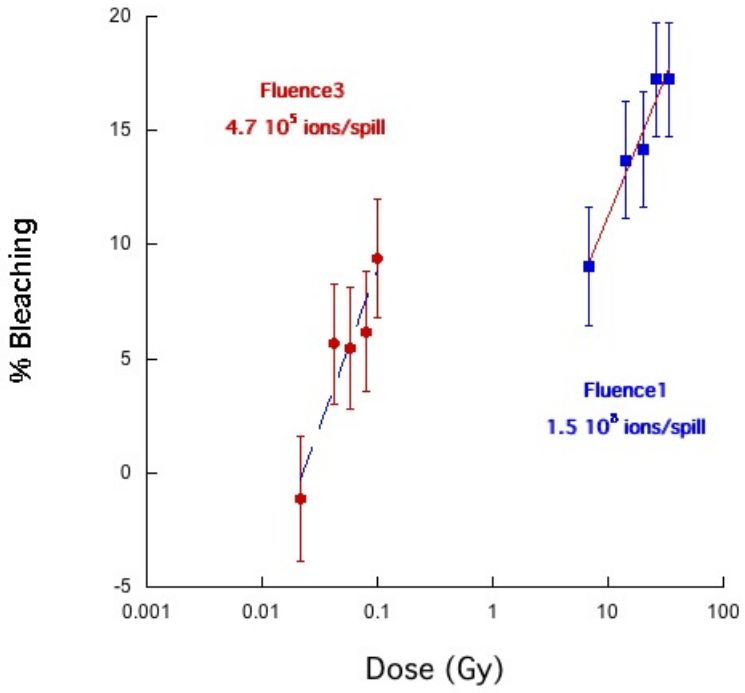

Figure 5.11: Samples Super-1 for low (Fluence3) and high (Fluence1) fluences.

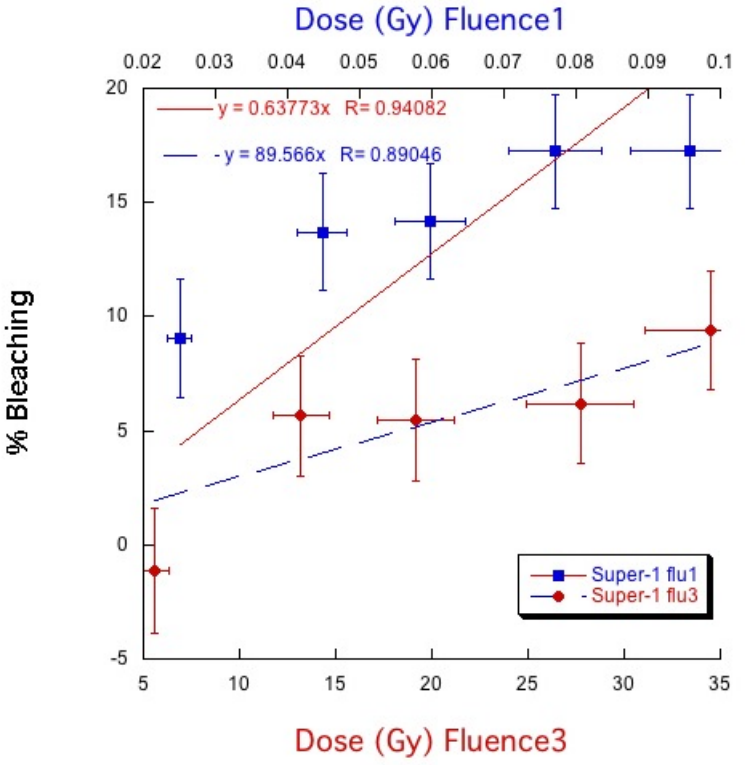

Figure 5.12: Samples Super-1 for low (Fluence3) and high (Fluence1) fluences.

factor ≈ 140. This results is not correlated with the different concentration of the rhodopsin, because all the samples in figures 5.11 and 5.12 belong to the group Super-1.

The different trends at the different fluences cannot be imputable to the recombination of the free radicals which originate the bleaching, as discussed in the section 4.7. Now we take into consideration the general concept of dose, defined in section 4.2. Although defined at each point of a certain volume, as a local information, the absorbed dose can be considered a *macroscopic* quantity, because its value is averaged over microscopic fluctuations of energy deposition. However, these fluctuations are important, because they are the reason why equal dose of different types of radiation, or radiation delivered in different conditions, produce effects of different magnitudes.

Although the absorbed dose determines the average number of energy deposition events, each cell as an individual entity will react, in fact, to the actual energy deposited in it. The average response of a system of cells should therefore depend on the energy distribution on a scale that is at least as small as the dimensions of the cell.

In particular, in our case, the irradiated system is a sample of a suspension of ROS. ROS is a very special material, as described in the section 2.1: it consists of a stack of thousands of disks surrounded by a cell membrane. The dimension of this cellular segment is of tens of micrometers in length and around one micrometer in diameter. So the major fluence could correspond to a major concentration of free radicals inside the same cellular segment. In this case a very complex response to the irradiation may take place. Our data, and the particular methods and procedures applied to obtain them are not sufficient to investigate a possible effect which originates at a cellular level like this. So new kinds of experiments over a cellular systems of rods could be a new perspective to investigate the activation of rhodopsin photoreceptors caused by radiation inside the cells in greater detail.

Chapter 6

Radicals excess in the retina: a model for LF in space

Up to now some experimental evidences regarding the interaction between carbon ions and rods photoreceptor have been shown: the rhodopsin photoreceptor underwent activations (that is isomerization) under the effect of carbon ions at a relative energy of $200\,MeV/n$, as discussed in chapter 4. We also shown the fact that the data of the activations of rhodopsin molecules are compatible with an indirect effect of radiation. An experimental evidence of interaction between irradiation and the visual system in the animal model is the fact that mice underwent a retinal/cortical physiological responses to a stimulation of carbon ions at $200\,MeV/n$, as described in chapter 2.

This chapter explains that the beaching of the rhodopsin as an indirect product of the irradiation and provides the possibility to propose a model for LF origin.

In particular this chapter is devoted to show the specificity of rhodopsin, as a membrane protein surrounded by the phospholipids of the membrane and to show that the recombination of radicals produced by heavy ions and high energy particles targeting polyunsaturated fatty acids (PUFA) around rods outer segments (where polyunsaturated fatty acids were found present abundantly) generates photons in a wavelenght range of approximatley $(420 \div 500)\,nm$ suitable to bleach rhodopsin. The photon capture, in fact, leads to photoisomerization of the $11-cis$ to $all-trans$ form of the chromophore (as explained in section 2.1), that is the primary event in

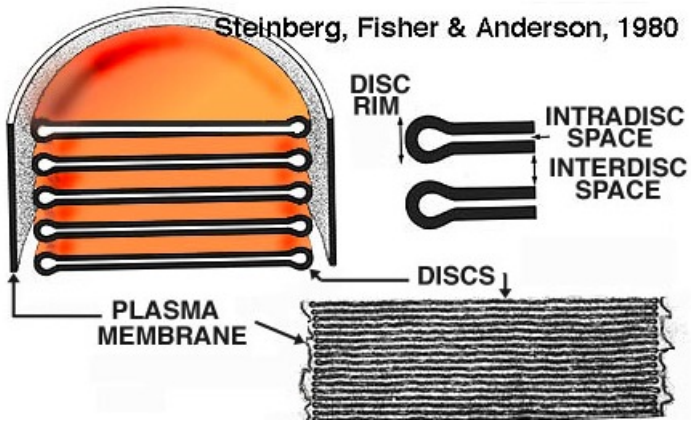

Figure 6.1: Disks in a ROD.

visual signal transduction, and is the only light-dependent step [48].

6.1 Lipid peroxidation in disk membrane of rod

The disk membranes consist of a large content of protein compared to plasma membranes resulting in a protein: lipid ratio by weight of 60% protein: 40% lipid. Of the protein in the membrane, more than 95% consists of rhodopsin. This ensures that there is a very large concentration of the protein that is responsible for the absorption of photons and a resulting signal in the bipolar neuron, which thereby maximizes the strength of the response to light excitation of retinal. Most of the lipids in the disk membranes are unsaturated, with many highly unsaturated lipids. The retinal disk is often described as being fluid, meaning that there is a large amplitude and rate of motion of the lipid chains. Cholesterol generally reduces the fluidity of membranes but in the disk membranes, there is only a small content, which therefore also helps ensure that there is a high fluidity. The high fluidity of the membrane means that it is much easier for the rhodopsin protein to undergo a conformational change since it is not restricted by a rigid membrane. Disks are known to be inside-out membranes with the rhodopsin oligosaccharide group present on the inside of the disc. The lipids are also asymmetric with phosphoethanolamine on the disk outer side and phosphatidylcholine on the inner disk side, which is normal for membranes, see figure 6.1.

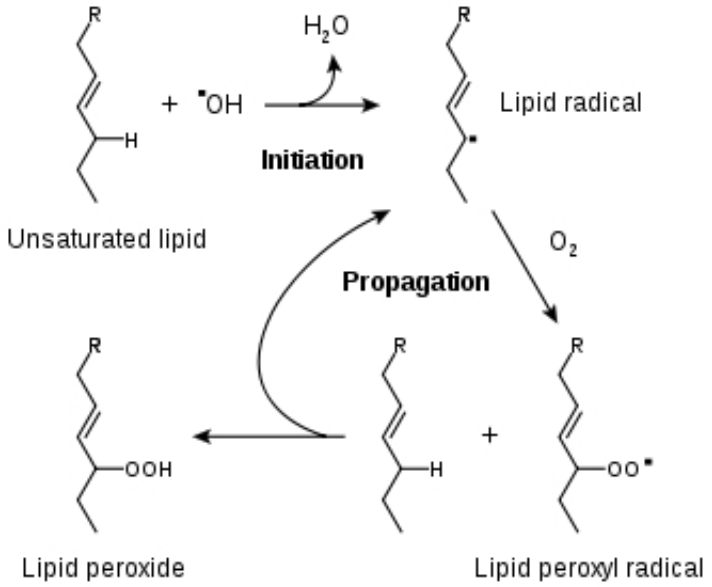

Figure 6.2: Mechanism of lipid peroxidation.

All cellular membranes are especially vulnerable to oxidation due to their high concentration of polyunsaturated fatty acids (PUFA) which are abundant in nature [49].

The lipid peroxidation of PUFA can be enzymatic and non-enzymatic. Lipid peroxidation is generally thought to be a major mechanism of cell injury in aerobic organisms subjected to oxidative stress. Among cellular macromolecules, polyunsaturated fatty acids (PUFAs) exhibit the highest sensitivity to oxidative damage. It is accepted that their sensitivity increases as a power function of the number of double bonds per fatty acid molecule. Membrane phospholipids are particularly susceptible to oxidation not only because of their highly polyunsaturated fatty acid content but also because of their association in the cell membrane with non-enzymatic and enzymatic systems capable of generating prooxidative-free radical species. In figure 6.2 a scheme shortly illustrates the mechanism of lipid peroxidation.

Figure 6.3 shows a schematic diagram of the non-enzymatic lipid peroxidation of docosahexaenoic acid 22:6n-3, a major dietary $\omega - 3$ PUFA and a major structural lipid of retinal photoreceptor outer segment membranes.

There are two broad outcomes to lipid peroxidation: structural damage to mem-

branes and generation of secondary products. Membrane damage derives from the generation of fragmented fatty acyl chains, lipidlipid cross-links, lipidprotein cross-links and endocyclization to produce isoprostanes and neuroprostanes. Thus lipid peroxidation of long chain polyunsaturated fatty acids such as arachidonic acid (C20:4n-6) and docosahexaenoic acid (C22:6n-3) produce isoprostanes and neuroprostanes, respectively. These processes combine to produce changes in the biophysical properties of membranes that can have profound effects on the activity of membrane-bound proteins. The consequence of peroxidation of unsaturated fatty acids is severe: damage of membranes function, enzymatic inactivation, toxic effects on the cellular division, etc., [49] and references therein.

Nevertheless, here we are specifically interested on outer segments of photoreceptors and light emission, obtained via non-enzymatic lipid peroxidation.

Non-enzymatic lipid peroxidation is a free radicaldriven chain reaction in which one radical can induce the oxidation of a large number of lipid molecules (LH) mainly phospholipids containing polyunsaturated fatty acids (PUFA). Such a chain reaction is initiated by the abstraction of a hydrogen atom from a cis interrupted methylene group of a PUFA residue.

Initiation is usually performed by a radical ($\mathbf{R^\bullet}$) of sufficient reactivity:

$$\mathbf{LH + R^\bullet} \quad \longrightarrow \quad \mathbf{L^\bullet + RH} \tag{6.1}$$

Molecular oxygen rapidly adds to the carbon-centered lipid radical ($\mathbf{L}$) formed in this process, yielding lipid peroxyl radical ($\mathbf{LOO^\bullet}$):

$$\mathbf{L^\bullet + O_2} \quad \longrightarrow \quad \mathbf{LOO^\bullet} \tag{6.2}$$

which, in turn, can abstract a hydrogen from another PUFA, similarly to 6.1:

$$\mathbf{LH + LOO^\bullet} \quad \longrightarrow \quad \mathbf{L^\bullet + LOOH} \tag{6.3}$$

Reaction 6.3 is named propagation, implying that one initiating hit can result in the conversion of several PUFA molecules to lipid hydroperoxides.

Lipid hydroperoxide (LOOH) is the first, relatively stable, product of the lipid peroxidation reaction. Under conditions where lipid peroxidation is continuously

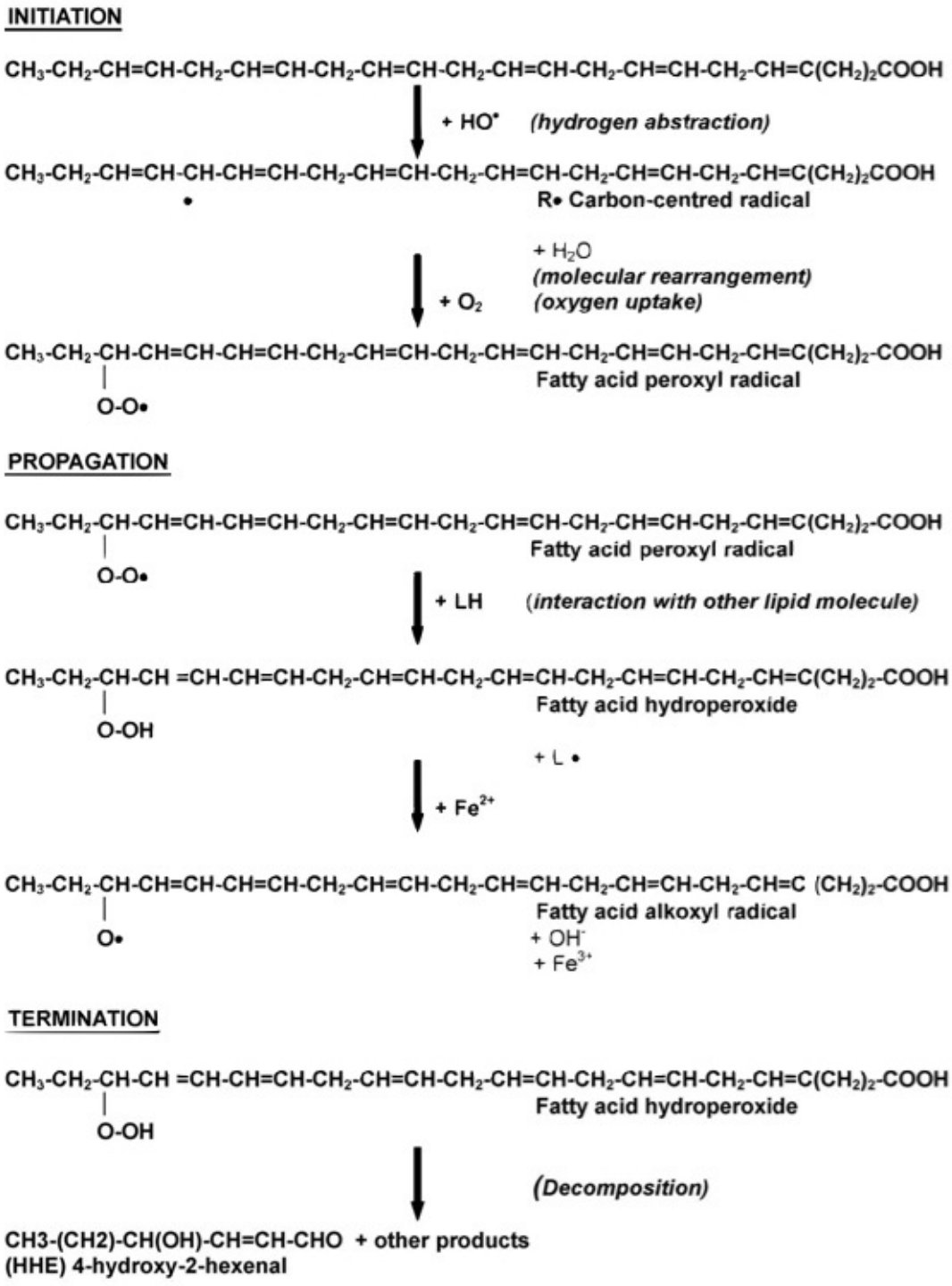

Figure 6.3: Lipid peroxidation of docosahexaenoic acid (22:6n-3). From [49]

initiated, a termination reaction limits the extent of this process, yielding non-radical products (NRP), and destroying two radicals at once:

$$\mathbf{LOO^{\bullet}} + \mathbf{LOO^{\bullet}} \quad \longrightarrow \quad \mathbf{NRP} \tag{6.4}$$

6.2 The mechanism of lipid peroxidation is associated with light emission

Lipid peroxidation is followed by a chain reaction that includes initiation, propagation and termination. Initiation occurs when an oxidant gives rise to an initiating lipid peroxyl radical (**LOO$^{\bullet}$**) by reaction with either a lipid (**LH**) or preexisting lipid hydroperoxide (**LOOH**). Lipid peroxidation termination involves the reaction of two **LOO$^{\bullet}$** to form non-radical products or the reaction of one **LOO$^{\bullet}$** with another terminating radical to generate non-propagating radical species; this reaction is particularly interesting since it is accompanied by emission of light: chemiluminescence.

$$\mathbf{LOO^{\bullet}} + \mathbf{LOO^{\bullet}} \quad \longrightarrow \quad \mathbf{P}^{*} \quad \rightarrow \quad \mathbf{P} + \phi h\nu \tag{6.5}$$

Chemiluminescence is a collective term considering the emission of light by molecules, which have been excited to a higher energy level as a result of a chemical reaction.

Bleaching from radical induced chemiluminesce

An *ad hoc* test was designed to document that rhodopsin can be bleached by chemiluminescence. A xanthine/xanthine oxidase reaction was used to generate radicals in the presence of triglycerides (4%) in a ultra thin optically polished, glass tube. This was positioned in a cuvette containing the rod outer segments preparation, so that only the chemiluminescent photons could reach the photoreceptors, while lipid and radicals were kept separated from them.

In detail, to analyse these effects of radical species on ROS suspension ($0.25\,\mu g/\mu l$), we used the xanthine 1.2 mM/xanthine oxidase 0,6U/ml system which is able to gen-

erate $0.52\mu MO_2^{*-}/min$ [33]. This reaction was repeated several times by addition of xanthine/xanthine oxidase system (Sigma) on the same sample and then it was spectrophotometrically analysed to check its absorbance at 500 nm.

The figure 6.4 refers to an experiment performed adding the xanthine/xanthine oxidase system to a solution containing PUFAs (olive oil 4-5% and fish oil 4%), solubilized with a suitable detergent (SDS 10%), physically separated from the ROS sample. The ROS sample was stored in a spectrophotometric cuvette while the reaction between PUFAs solution and xanthine/xanthine oxidase occurred in a ultrathin optically polished NMR glass tube inserted in the cuvette.

We found that rhodopsin bleaching was proportional to the radicals concentration (figure 6.4) and full regeneration was possible.

When the experiment was repeated with no separation between rod outer segments and radicals, the rod segments were damaged and bleached rhodopsin could not be regenerated. Increased lipid concentration enhanced bleaching which became negligible when antioxidants were added.

6.3 Discussion

In summary the results exposed in this chapter can be represented in the schema of figure 6.5.

In the figure we present schematically a model for the generation mechanism of the light flashes in space, this model is supported by the results of in vitro tests exposed in this chapter. The model can be a common end point for the interactions between ionizing radiation and visual system in space. It would also support the assessment of functional radiation risks in space.

In figure 6.5 the model is described in four steps. Every step has been discussed and illustrated in detail in the preceding. Two of the four steps (2 and 3, continuous blue arrows) are supported by previously published evidences ([46], [49]). The two red dashed arrows indicated the experimental validation of the model presented in this thesis: we tested in vitro the whole sequence of events (ionizing radiation, namely ^{12}C, induces rhodopsin bleaching), and the fourth step (chemiluminescence

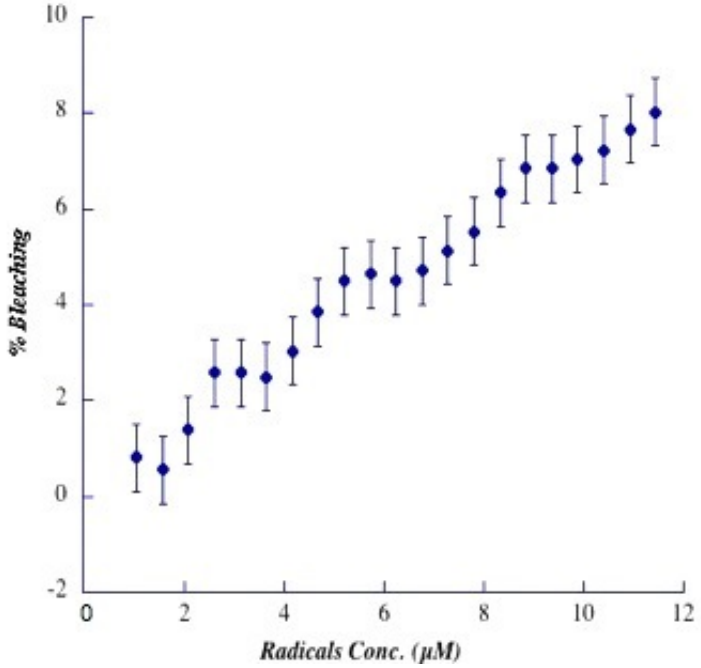

Figure 6.4: Rhodopsin bleaching in percentage vs radicals concentration obtain adding xanthine/xanthine oxidase to a solution of olive oil $(4-5\%)$ and fish oil (4%). The ROS in suspension and the solution containing the oils are separated by a transparent surface.

from lipid peroxidation induces rhodopsin bleaching).

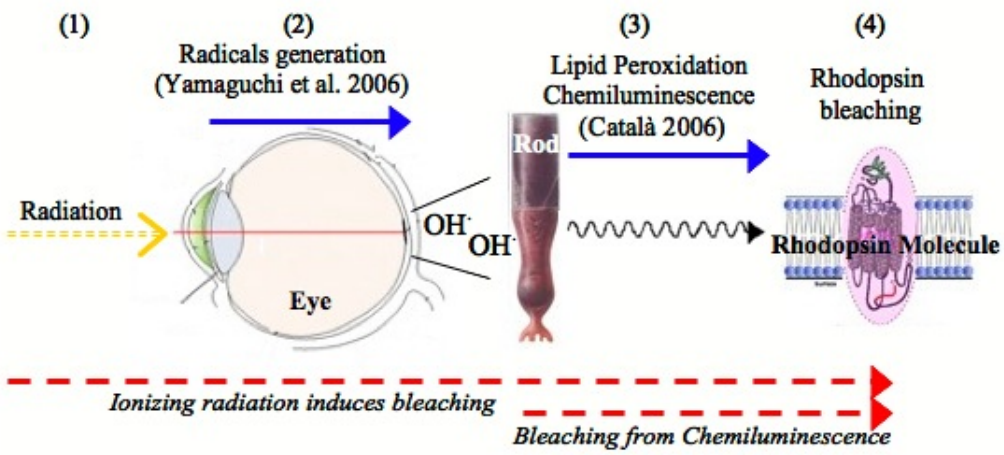

Figure 6.5: Four step model for Light Flash generation: (1) the ionizing radiation is impinging in the eye; (2) radicals are generated in the eye; most of them are quenched; (3) some of the radicals generated in the rod lipids undergo lipid peroxidation which result in chemiluminescence, and in the emission of a photon; (4) the photon bleaches a nearby rhodopsin: the photo- transduction cascade is started, a light flash can be perceived. The red dashed arrows indicate the presented experimental tests. From [3]

From the results reported here it appears that ions traveling near the retina may start the process generating light flashes at proper threshold. Our study suggests a manner to generate LF following the passage of a charged particle in the retina. We can't exclude other kinds of LF generations, and one of the aim of ALTEA project are devoted to better investigate this topic.

The correlation between the yields of reactive free radicals and the activation of rhodopsin photoreceptors is linked to other considerations as - among others - to the number of unquenched radicals near the retina and thus depends on antioxidant concentration and, by extension, on individual factors (stress, fatigue, diet, etc). This can be a possible explanation for the large variability in rate of perception and shape of light flashes in orbit as reported by astronauts, and on ground the carbon ion threshold for and variability of retinal activation in mice.

This model is therefore compatible with the light flashes observed in space and may be the end point of different interactions between ionizing radiation and visual system, either direct (ions hitting the retina) or indirect. In this perspective, the light flashes observed by astronauts in space would signal for an excess of free radicals in or near the retina. In spite of its focusing on retinal phenomena, this model may also be a preliminary step in the assessment of risks related to the perception of phosphenes in space. A study [50] that collects historical data for cataract incidence in the 295 astronauts participating in NASAs Longitudinal Study of Astronaut Health, assets that astronauts on Apollo and subsequent Skylab, space shuttle, and Mir missions have observed light flashes that raise a concern for adverse tissue effects from single heavy-ion tracks. In the cited study preliminary results have been reported that indicate that low doses of space radiation increase the risk for cataracts, with possible implications for future space missions including the International Space Station and missions returning to the moon or exploring Mars. This report - as other similar reports on the safety of astronauts - suggests that damage from ionizing radiation can cause adverse tissue effects in a dose- and LET-dependent manner that will require further study to understand the mechanisms and the nature of such risks for space travel.

Chapter 7

Conclusions and future development

In this thesis are described and discussed the experimental set-up and the main results of ALTEA-MICE and ALTEA-biophys, which are two of the ALTEA project sections devoted to the experiments on ground. An important part of my work was aimed to the realization of the experiments and to the analysis of the data.

For the preparation of the ALTEA-MICE experiments we realized an experimental apparatus and a reproducible procedure to irradiate the eye of the mice in controlled conditions and to record the retinal and cortex signals following the proper electrophysiological requirements. An important result is the experimental evidence of an electrophysiological response of the mice irradiated with carbon ions at a relative energy of $200\,MeV/n$, as described in chapter 3.

Concurrently the effects of radiation on the photoreceptor of the rods have been investigated. The preparation of the sample containing the rod outer segments of bovine retinae in suspension was realized in the Biology Department of this university, while the irradiation of the samples were performed at the GSI accelerator at Darmstadt, in Germany and the analysis were performed in Physics Department. The preparation, the proper storage, the irradiation, the regeneration and the data analysis represent a tested and reproducible procedure which could be used for future investigations. The experiments on the rhodopsin irradiation lead to the conclusion that carbon ions at $200\,MeV/n$ are able to bleach the chromophore, that is that

heavy ions could activate the process of vision. We also found the evidence that the bleaching is an indirect effect of radiation. All the details of these experiments are illustrated in chapter 2 and chapter 5.

According to these results and to the available evidence that heavy ions generate free radicals in living tissue, we designed and tested a model of initiation of the process generating light flashes. In chapter 6 this model is described:

> *the high concentrations of lipids around the outer portion of photoreceptors and of radicals in the particle track increase the probability that radicals and lipids interact and give rise to lipid peroxidation. Lipid peroxidation is known to produce photons in the visible band, which are absorbed by intact nearby rods causing the bleaching of the rhodopsin and the starting of the photo-transduction cascade.*

ALTEA-MICE and ALTEA-biophys series of experiments provide tested and reproducible procedures also for future measurements. In vivo experiments on mice will be possibly replicated under experimental conditions allowing the addition of compounds with anti-oxidant properties, to monitor the possible effects and to identify possible countermeasures. It could be investigated the interaction between heavy ions and the intracellular calcium concentration and the possible consequence on the transduction cascade in the outer segment. It could be studied the extent to which calcium signaling can reflect rod outer segment repair dynamics upon damage due to radical peroxidation. The results would also be useful to plan bio-countermeasures for the radicals-induced damage of the retina.

Bibliography

[1] W. G. Sannita, **A. Rinaldi**, *et al.*, *Electrophysiological responses of the mouse retina to ^{12}C ions*,
Neuroscience Letters, 2007, **416**, 231235.

[2] W. G. Sannita, **A. Rinaldi**, *et al.*, *Effects of heavy ions on visual function and electrophysiology of rodents: the ALTEA-mice project*,
Advances in Space Research, 2004, **33**/8, 1347-1351.

[3] L. Narici, A. De Martino, V. Brunetti, **A. Rinaldi**, W. G. Sannita, and M. Paci, *Radicals excess in the retina: a model for Light Flashes in space*,
Rad. Meas. *S1350-4487(09)00007-9* RM 3657.

[4] L. S. Pinsky, W. Z. Osborne,J. V. Bailey, R. E. Benson and L. F. Thomson, *Light Flashes Observed by Astronauts on Apollo 11 through Apollo 17*,
Science, 1974, 183 : 957-959.

[5] Y. Akatov, *et al.*, *Biomedical aspects of Light Flashes observed by Astronauts during Space Flight*,
Proceedings of the 6^{th} European Symposium on Life Science Research in Space, ESA SP-390, October 1996.

[6] K. D. Steidley, *The Radiation Phosphene*,
Vision Res., 1990, **30**, 8, 1139-1143.

[7] P. J. McNulty, *et al.*, *Visual sensations induced by relativistic nitrogen nuclei*,
Science, 1972, **178**, 160-161.

[8] L. S. Pinsky, W. Z. Osborne, *Light Flashes Observed by Astronauts on Skylab4*, Sciece, 1975, **188**, 928-930.

[9] L. Narici, *Heavy ions light flashes and brain functions: recent observations at accelerators and in spaceflight*, New Journal of Physics, 2008, **10**, 075010.

[10] M. Casolino, *et al.*, *Dual origin of light flashes seen in space*, Nature, 17 April 2003, **22.**

[11] W. G. Sannita, L. Narici, P. Picozza, *Positive visual phenomena in space: A scientific case and safety issue in space travel*, Vision Res., 2006, **46**, 2159-2165.

[12] S. Avdeev, *et al.*, *Eye light flash on the Mir station*, Acta Astronautica, 2002, **50**, 511-525.

[13] L. S. Pinsky, *et al.*, *Light Flashes Observed by Astronauts on Apollo 11 through Apollo 17*, Science, 1974, **183**, 957-959.

[14] R. A. Hoffman, L. S. Pinsky, W. Z. Osborne and J. Z. Bailey, *NASA Report*, SP-377, 1977, 127-130.

[15] T. F. Budinger *et al.*, *NASA Report*, SP-412, 1977, 193-209.

[16] C. Fuglesang, L. Narici, P. Picozza and W. G. Sannita, *Phosphenes in Low Earth: Survey Responses from 59 Astronauts*, Aviation, Space, and Environment Medicine, April 2006, **77**-4, 449-452.

[17] M. Casolino, *Radiation in Space: causes, measures and countermeasures*, Frascati Physics Series, Vol. XXIV (2002), 195-216.

[18] M. Casolino, *et al.*, *Light Flashes Observations on Board Mir and ISS with SilEye Experiments*, 28th Int. Cosmic Ray Conference, 2003, pp. 4161-4164.

[19] M. Casolino, *et al.*, *Relative Nuclear Abundances Measuremaents inside Mir and ISS with SilEye-2 and SilEye-3 Experiments*,
28th Int. Cosmic Ray Conference, 2003, pp. 4245-4248.

[20] L. Narici *et al.*, *The ALTEA/ALTEINO projects: studying functional effects of microgravity and cosmic radiation*,
Advances in Space Research, 2004, **33**, 1352-1357.

[21] V. Bidoli, *et al.*, *ALTEA - A facility to study the interaction of brain functionality and visual system with cosmic radiation on ISS*,
Proceedings of the 2^{nd} European Symposium on the Utilization of the International Space Station, ESA_SP_433, February 1999.

[22] V. Zaconte, *et al.*, *ALTEA: the instrument calibration*,
Nucl. Instrum. Methods B, 2008, **266** 20702078.

[23] L. Narici, *et al.*, *The ALTEA facility on the International Space Station*,
Phys. Med., 2001, **17**, Suppl. 1.

[24] T. P. Sakmar, *Structure of rhodopsin and the superfamily of seven-helical receptors: the same and not the same*,
Current opinion in cell biology, 2002, **14**(2), 189-195.

[25] H. Kolb, *How the Retina Works*,
American Scientist, 2003, **91**, 28.

[26] T. P. Sakmar, S. T.Menon, E. P.Marin, and E. S. Awad, *Rhodopsin: Insights from Recent Structural Studies*,
Annu. Rev. Biophys. Biomol. Struct., 2002 **31**, 44384.

[27] P. A. Hargrave, and J. H. McDowell, *Rhodopsin and phototransduction: a model system for G-protein-linked receptors*,
The FASEB Journal, 1992, **6**, 2323-2331.

[28] D. C. Teller, T. Okada, C. A. Behnke, K. Palczewski, and R. E. Stenkamp, *Advances in Determination of a High-Resolution Three-Dimensional Structure*

of Rhodopsin, a Model of G-Protein-Coupled Receptors (GPCRs),
Biochemistry, 2001, **40**, No. 26.

[29] D. S. Papermaster, *Preparation of retinal rod outer segments*,
Methods Enzymol., 1982, **81**, 48-52.

[30] D. S. Papermaster, W. J. Dreyer, *Rhodopsin content in the outer segment membranes of bovine and frog retinal rods*,
Biochemistry, 1974, **21**, 13(11), 2438-44.

[31] D. Fotiadis, Y. Liang, S. Filipek, D.A. Saperstein, A. Engel, and K. Palczewski, *Atomic-force microscopy: Rhodopsin dimers in native disc membranes*,
Nature, 2003 **421**, 127-128.

[32] Fasman, D.G., **Practical Handbook of Biochemistry and Molecular Biology,**
Ed. (1992). CRC Press, Boston.

[33] L. Narici, M. Paci, V. Brunetti, A. Rinaldi, W. G. Sannita, and A. De Martino, *Luminescence from recombination of radicals from polyunsaturated fatty acids bleaches rodhopsin in bovin eye rods: a possible source for light flashes of astronauts in space*,
paper in preparation.

[34] W. R. Leo, **Techniques for Nuclear and Particle Physics Experiments**,
Springer-Verlag, Second Revised edition, 1993.

[35] J. Kiefer, **Biological Radiation Effects**,
Springer-Verlag.

[36] A. Mozumder, **Fundamental of Radiation Chemistry**,
Academic Press, 1999.

[37] G.Kraft and M. Krämer, *LET and track structure*,
Adv. Radiat. Biol., 1993, **17**, 1-52.

[38] G.Kraft, *Radiobiological effects of highly charged ions*,
The Physics of Highly and Multiply Charged Ions, Ed. F. J. Currel Kluwer Academic Publisher 2002.

[39] J. Kiefer, *The physical basis for the biological action of heavy ions*,
New journal of physics, 2008 **10**, 075004.

[40] H. Nikjoo, S. Uehara, D. Emfietzoglou and A. Brahme, *Heavy charged particles in radiation biology and biophysics*,
New journal of physics, 2008 **10**, 075006.

[41] J. Kiefer and H. Straaten, *A model of ion track structure based on classical dynamics*,
Phys. Med. Biol., 1986, **11**, 1201-1209.

[42] T. Elsässer, R. Cunrath, M. Krämer and M. Scholz, *Impact of track structure calculations on biological treatment planning in ion radiotherapy*,
New journal of physics, 2008 **10**, 075005.

[43] K. Gunzert-Marx, H. Iwase, D. Schardt and R. S. Simon, *Secondary beam fragments produced by 200 MeV/μ ^{12}C ions in water and their dose contributions in carbon ion radiotherapy*,
New journal of physics, 2008 **10**, 075003.

[44] S. Borons, G. Taucher-Scholz, M. Scholz, G. Kraft, *A track structure model for simulation of strandbreaks in plasmid DNA after heavy ion irradiation*,
Radiat. Environ. Biophys, 2003 **42**, 63-72.

[45] V. Moiseenko, R. Hamm, A. Waker and W. Prestwich, *Calculation of radiation-induced DNA damage from photons and tritium beta-particles. Part I: Model formulation and basic results*,
Radiat. Environ. Biophys, 2001 **40**(1), 23-31.

[46] H. Yamaguchi, Y. Uchihori, N. Yasuda, M. Takada and H. Kitamura, *Estimation of yields of OH radicals in water irradiated by ionizing radiation*,
J. Radiat. Res., 2005, **46**, 333-341.

[47] D.Swiatla-Wojcik and G. V. Buxton, *Modelling of linear energy transfer effects on track core processes in the radiolysis of water up to* 300^0C,
J. Chem. Soc., Faraday Trans., 1998, **94**(15), 2135-2141.

[48] G. Wald, *Molecular basis of visual excitation*,
Science, 1968, **162**, 230-239.

[49] A. Catalá, *An overview of lipid peroxidation with emphasis in outer segments of photoreceptors and the chemiluminescence assay*,
The International Journal of Biochemistry Cell Biology, 2006, **38**, 14821495.

[50] F. A. Cucinotta *et al.*, *Space Radiation and Cataracts in Astronauts*,
Radiation Research, 2001, **156**, 460466.

Acronyms

ALTEA Anomalous long Term Effect on Astronauts

ASI Italian Space Agency

ASTP Apollo-Soyuz Test Project

BNL Brookhaven National Laboratories

CNS Central Nervous System

CNSM Central Nervous System Monitoring

EEG ElectroEncephaloGrapher

ERG ElectroRetinoGram

ESA European Space Agency

GSI Gesellschaft fur Schwerionenforschung mbH

INFN National Institute for Nuclear Physics

ISS International Space Station

LEM Local Effect Model

LEO Low Earth Orbit

LET Linear Energy Transfer

LF Light Flash(es)

MICE Mice intermittent Irradiation with Concurrent Electrophysiological monitoring

PUFAs Polyunsaturated Fatty Acids

NASA National Space Agency

RET Retinal

ROS Rod Outer Segment

SAA South Atlantic Anomaly

VEP Visual Electrode Potential